Measurement of cumulative photofission yields of ^{235}U and ^{238}U with a 16 MeV Bremsstrahlung photon beam

Manon Delarue, E. Simon, B. Pérot, P.G. G Allinei, N. Estre, E. Payan, D. Eck, D. Tisseur, Isabelle Espagnon, J. Collot

Journal Pre-proof

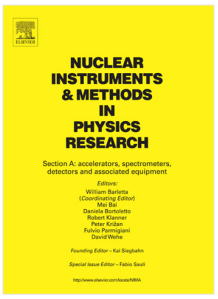

Measurement of cumulative photofission yields of ^{235}U and ^{238}U with a 16 MeV Bremsstrahlung photon beam

M. Delarue, E. Simon, B. Pérot, P.G. Allinei, N. Estre, E. Payan, D. Eck, D. Tisseur, I. Espagnon, J. Collot

PII: S0168-9002(21)00583-0
DOI: https://doi.org/10.1016/j.nima.2021.165598
Reference: NIMA 165598

To appear in: *Nuclear Inst. and Methods in Physics Research, A*

Received date : 4 March 2021
Revised date : 3 June 2021
Accepted date : 28 June 2021

Please cite this article as: M. Delarue, E. Simon, B. Pérot et al., Measurement of cumulative photofission yields of ^{235}U and ^{238}U with a 16 MeV Bremsstrahlung photon beam, *Nuclear Inst. and Methods in Physics Research, A* (2021), doi: https://doi.org/10.1016/j.nima.2021.165598.

Measurement of cumulative photofission yields of ^{235}U and ^{238}U with a 16 MeV Bremsstrahlung photon beam

M. Delarue[1*], E. Simon[1], B. Pérot[1], P.G. Allinei[1], N. Estre[1], E. Payan[1], D. Eck[1], D. Tisseur[1], I. Espagnon[2], J. Collot[3]

[1] CEA, DES, IRESNE, DTN, SMTA, Nuclear Measurement Laboratory, F-13108 St Paul-lez-Durance, France

[2] Université Paris-Saclay, CEA LIST, F-91120 Palaiseau, France

[3] Grenoble INP, LPSC-IN2P3, 38000 Grenoble, France

[*]Corresponding author: manon.delarue@cea.fr

Keywords

Photofission, uranium, delayed gamma rays, Bremsstrahlung, fission yield, photon activation analysis, MCNP

Abstract

In the frame of a long-term research program on the characterization of large radioactive waste packages by photofission, the Nuclear Measurement Laboratory of CEA IRESNE, France, has measured cumulative photofission yields of ^{235}U and ^{238}U short-lived and long-lived fission products by using a Bremsstrahlung photon beam produced by a 16 MeV electron linear accelerator (LINAC). To this aim, a characterization of the Bremsstrahlung photon beam has been carried out by photon activation analysis with different samples of gold, nickel, uranium and zirconium. The residual neutron flux exiting the LINAC head (lead collimator, borated polyethylene and cadmium shield) has also been characterized by neutron activation analysis with indium samples to estimate the contribution of photoneutron fissions in the uranium samples used to assess the

photofission yields. Finally, 49 fission product yields are reported for ^{238}U and 26 for ^{235}U, with half-lives ranging from 64 s to more than 3 days, some of them not recorded so far in the literature. Some photofission products cumulative yields show significant differences between ^{235}U and ^{238}U, which confirms the possibility of an isotopic discrimination method based on delayed gamma-ray ratios analysis for radioactive waste characterization.

1. Introduction

The management of radioactive waste (transportation, interim storages and final repositories) needs an accurate characterization of their nuclear material content. Among many non-destructive methods that have been studied to address this characterization, active interrogation methods are necessary for large and dense packages, such as concrete drums [1]-[4]. Specifically, Active Photon Interrogation (API), based on the detection of delayed gamma radiation emitted by fission products induced by high-energy photons, has the potential to assess the nuclear material mass present in a package, and possibly to distinguish fertile and fissile isotopes (e.g. ^{238}U and ^{235}U, respectively) using a discrimination signal based on their delayed gamma rays. The detection of delayed gamma rays with a high-purity germanium (HPGe) detector has the potential to measure the production yields of fission products with an accuracy lower than 5 %, enabling the differentiation from one isotope to the other [1].

However, nuclear data related to photofission yields are scarce and the reported fission product cumulative yields show significant discrepancies, even for recent studies [5]-[11]. Due to the Giant Dipolar Resonance (GDR), the photofission cross-section of both odd and even mass number actinides (e.g. ^{238}U and ^{235}U) are of the same order of magnitude, contrary to thermal neutron fission for which they differ by several decades. Uranium 235 is a “fissile” actinide (in the sense of thermal neutron fission) of first interest in a radioactive waste, but it is most of the time accompanied with a 10 to 100 times larger mass of uranium 238. Even with well-known photofission cross-sections, relative fission product yields of these two uranium isotopes have to be determined with a good accuracy in view of their discrimination.

Several research groups have shown the potential of measuring delayed gamma rays following fission for the differentiation of actinides, such as Hollas *et al.* [12] for photofission, Beddingfield [13] for thermal neutron fission, with the use of delayed gamma-ray ratios for actinide identification. Further experimental work was conducted by Gmar *et al.* [14], pointing out variations of the delayed gamma-ray emissions for uranium samples of different enrichments. Carrel *et al.* [1] have investigated delayed gamma emission following photofission in mixed samples of ^{235}U and ^{238}U, and delayed gamma-ray ratios for actinide differentiation with samples positioned in the center of an 870 L mock-up package. Simon *et al.* have also reported the possibility to distinguish uranium 235 and 238 in 870 L radioactive waste packages using Monte-Carlo simulations [4], by comparing the intensities of gamma rays from photofission products with close energies, for centered and peripheral sample locations.

We present here the first experimental step of the development of a method using photofission as a probe to quantify the fissile mass in large volume heterogeneous radioactive waste packages, which aims at producing cumulative photofission yields for the fission products of ^{235}U and ^{238}U, and identifying fission products of interest for ^{235}U vs. ^{238}U discrimination. Fission products emitting several gamma rays could be used as attenuation indicators to estimate the depth at which nuclear materials are localized inside the package. In this way, attenuation corrections could be applied to avoid using only close-in-energy gamma rays for the discrimination method. The attenuation corrections according to the depth of nuclear materials in the package, also known as matrix and localization effect corrections, are also needed for the final assessment of their mass and constitutes a challenge in large, dense and heterogeneous radioactive waste packages.

This paper presents the experimental setup deployed at CEA Cadarache using a high-energy electron LINAC in the CINPHONIE casemate of the CHICADE facility [15], uranium samples and a high-resolution gamma-ray spectrometer. The experimental and numerical methods used to characterize the interrogating photon beam are then described, as well as the neutron spectrum, by photon and neutron activation analysis, respectively. These data are crucial to finally obtain data on 26 and 49 cumulative photofission yields for respectively ^{235}U and ^{238}U fission products, which are presented at the end of this paper.

2. Experimental setup

Experiments were performed by using a Bremsstrahlung photon beam produced by a LINAC located in the CINPHONIE irradiation cell at CEA Cadarache. This SATURNE accelerator initially designed for medical treatments has two accelerating cavities. It has been restored in the past few years in order to meet dose rates and Bremsstrahlung endpoint-energies required by high-energy photon imaging and photofission experiments on large and dense radioactive waste packages. At the time of the experiments presented in this paper, the LINAC was operated in degraded mode and the dose rate at 1 m from the conversion target in the beam axis reached only a few Gy/min (since, it has been upgraded up to several dozens of Gy/min). In pulse mode, the LINAC accelerates electrons up to more than 15 MeV. The electrons strike a tungsten target and a part of their kinetic energy is converted into Bremsstrahlung radiation. The pulse frequency is up to 100 Hz with a pulse width of 4.1 µs and a peak current of 10 mA at the target entrance. Furthermore, a 20 cm thick lead collimator with two rectangular apertures, of dimensions 6.5 cm in width and 5.5 cm in height for the largest and 12 cm in width and 1.5 cm in height for the narrowest, allows focusing the beam on the uranium samples (see further Figure 1). With this setup, however, the photon flux at the output of the collimator aperture is not known precisely, nor is the endpoint-energy of the Bremsstrahlung spectrum, which is expected to be around 15 MeV. Therefore, a characterization of the photon beam produced by the LINAC, using photon activation of reference materials, is detailed in section 3. The tungsten Bremsstrahlung conversion target is a 5 mm thick cylinder with a 4 mm radius, placed perpendicularly to the incident electron beam. The tungsten target and the lead collimator of the LINAC can both produce photoneutrons by (γ,n) reactions when irradiated by high-energy photons. The (γ,n) reaction threshold energies range from 6.19 MeV to 8.07 MeV for tungsten isotopes and from 6.74 MeV to 8.09 MeV for lead isotopes [16]. The photoneutron flux expected at the location of the uranium sample could cause undesired neutron reactions in addition to photofissions, such as neutron fissions that can increase the delayed gamma emission and lead to an overestimation of the cumulative photofission yields, or neutron captures forming activation products that can emit delayed gamma rays constituting of an additional background. To limit the number of photoneutrons reaching

the uranium sample, a borated polyethylene (BPE) and polyethylene (PE) shield made of 20 cm thick blocks has been implemented all around the lead collimator (see Figure 5). The photon beam attenuation in 20 cm of polyethylene decreases the photofission rate in the samples by a factor 1.7. In order to complete the thermal neutron absorption occurring in the BPE shield, a cadmium layer of 2 mm was added on the front face. The simulated model of the LINAC with the associated collimator and neutron shielding is shown in Figure 1.

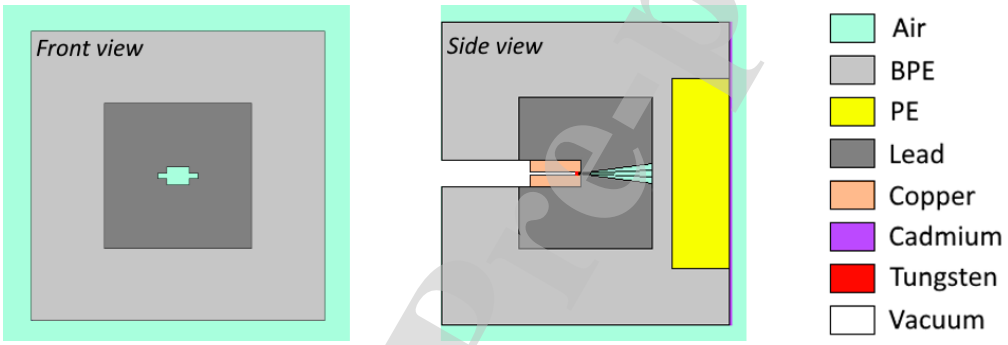

Figure 1: MCNP model of the collimator and of the neutron shielding surrounding the LINAC with the collimator aperture (left side) and the accelerating cavity as well as the tungsten target (right side)

A sample of Depleted Uranium (DU) of 99.7 % ^{238}U content, with a mass of several hundred grams and a sample of Highly Enriched Uranium (HEU), composed of more than 90 % of ^{235}U, with a mass lower than 1 g, were irradiated. The thickness and density of the DU metallic sample being respectively 1 cm and 18.96 g.cm^{-3}, significant self-attenuation effects occur both for the interrogating photon flux and the delayed gamma rays emitted by photofission products. Therefore, we apply correction factors in order to calculate the photofission product yields (see section 4.2). The second sample consists of a fissile HEU core, with a thickness well below 1 mm, a density of 18.96 g.cm^{3}, and zirconium separation wedges with a density of 6.52 g.cm^{-3}. In addition, the fissile core is held between two Zircaloy sheets of density 6.56 g.cm^{-3}. In radioactive waste, ^{235}U is generally mixed with ^{238}U and Figure 2 shows that the photofission cross-sections of these two isotopes are of the same order of magnitude. They reach only a fraction of barn and the cross-section of ^{235}U is approximately twice larger than that of ^{238}U, see Figure 3. The photofission cross-

section being very low compared to the thermal neutron fission cross-sections of fissile isotopes like ^{235}U (see Figure 3), we use a LINAC to provide a high interrogating photon flux. For incoming neutrons in the MeV energy range, however, the fission cross-section is similar for uranium 235 and 238, and it is only a few barns. As the aim of these experiments is to assess the photofission product yields as precisely as possible, we will estimate the residual contribution of neutron fissions in the uranium samples in section 4.1.

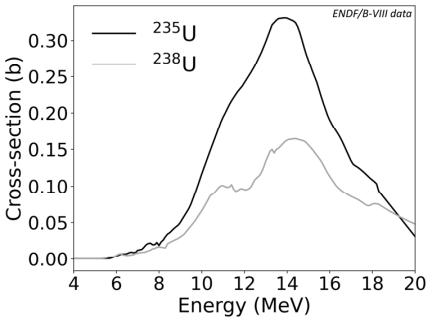

Figure 2: Photofission cross-sections of ^{235}U and ^{238}U [17]

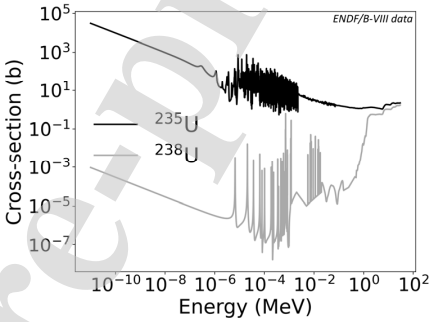

Figure 3: Neutron fission cross-sections of ^{235}U and ^{238}U [17]

To this aim, a set of thin metallic activation pellets was irradiated during 1 hour at 100 Hz at the same position as the uranium samples. These so-called "Neutron Activation Spectrometers" (French acronym "SNAC") shown in Figure 4 are pure metallic samples as described in Table 1. They will also be used to characterize the Bremsstrahlung beam by photon activation, namely the photon flux and its endpoint energy, in section 3.1.

Element	Mass (g)	Diameter (mm)	Thickness (mm)	Position on Figure 4
Au	0.045	5	0.05	1
In	2.711	22	1	2 & 4
Cu	1.731	22	0.5	3
Ni	10.027	22	3	5
Mg	6.599	22	10	6

Table 1: Characteristics of the neutron activation spectrometers

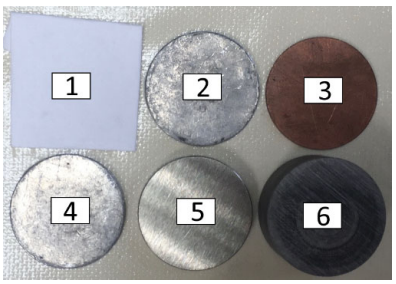

Figure 4: Position of the different materials with respect to the interrogating flux

The uranium samples were located at 43 cm from the LINAC tungsten target. They were fixed on the polyethylene sample holder visible in Figure 5, and irradiated one at a time. Then, an automatic transfer lasting 30 seconds, noted "cooling time" in further

activation analysis equations, was performed from the irradiation position to the counting position for both uranium samples. The transfer is done with a mechanical bench usually dedicated to high-energy photon tomography of radioactive waste packages in the CINPHONIE cell [18]. The samples used to characterize the Bremsstrahlung beam by photon activation were irradiated in the same position, but the transfer time to a low-background spectrometer located in another experimental room was longer. Table 2 summarizes the configuration related to each sample. Note that the LINAC frequency is lowered at 10 Hz (instead of 100 Hz) for the DU sample, resulting in an interrogating photon flux decreased by a factor 10 (same peak current but fewer pulses), in order to limit the dead time due to a high photofission delayed gamma-ray emission in this large sample.

Table 2: Experimental configurations

Sample	LINAC frequency	Irradiation time	Cooling time	Counting time
DU	10 Hz	2 h	30 s	67 h
HEU	100 Hz	2 h	30 s	22 h
Activation samples (Au, In, Cu, Ni, Mg)	100 Hz	1 h	40 min	43 h

In order to measure the fission and activation products created in the uranium samples, we use a 30 % relative efficiency n-type coaxial high-purity germanium detector (HPGe, CANBERRA GR3018) with a transistor-reset preamplifier, coupled to a LYNX Digital Signal Analyzer (CANBERRA) driven by the Genie2000 software (MIRION Technologies) also used for gamma spectra analysis. The energy resolution is 1.8 keV (FWHM) at the 1332.5 keV gamma line of ^{60}Co. Although an n-type HPGe crystal is used to limit neutron damage, the detector is shielded by lead and polyethylene, as shown in Figure 5. The uranium samples in their measurement position are located 20 cm away from the detector entrance surface to keep dead time below 30 %. The dead time compensation is a live-time correction. For the DU sample measurement, dead time right after the cooling period of 30 s was 29.7 % and gamma spectra are acquired sequentially every 60 s, with a spectrum reset at the start of each sequence. For the HEU sample measurement, the initial dead time is 4.21 % and spectra acquisitions are reset every 180 s. Consequently, it was

possible to follow and to correct for dead time according to its time evolution. The non-nuclear metallic samples used for the beam characterization were transferred inside a low-background spectrometer with a 10 % relative efficiency HPGe detector (CANBERRA BE2020) in a lead shield, with walls covered with a copper layer to cut lead X-rays. The detector is connected to a digital spectrometer (CANBERRA DSP9960) and the resolution is 1.75 keV (FWHM) at the 1332.5 keV gamma line of ^{60}Co. At the beginning of the activation pellets measurement, the dead time was very low (0.11 %).

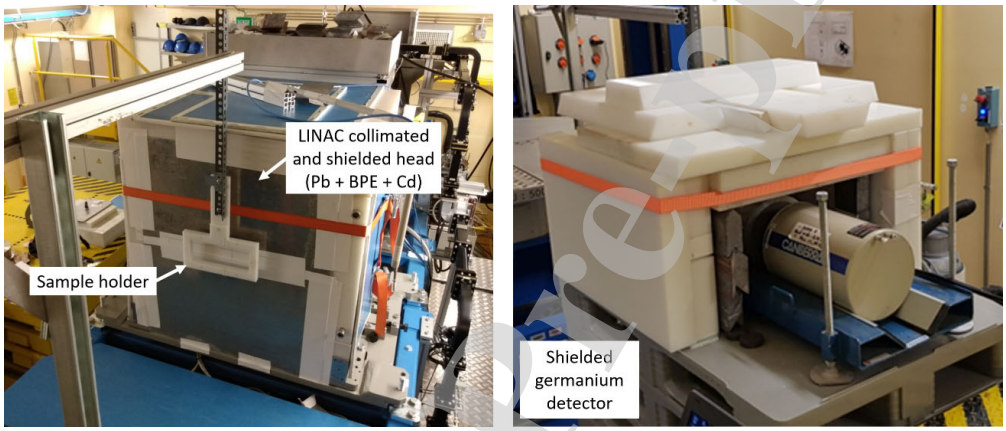

Figure 5: Experimental set-up inside the CINPHONIE casemate, with the head of the LINAC (left picture) and the HPGe detector (right picture)

3. LINAC beam characterization

3.1. Photon beam

The thin metallic samples initially intended to characterize the photoneutron flux (Au, In, Cu, Ni and Mg) finally proved to reveal also photon activation gamma rays. Their activation spectrum is presented in Figure 6.

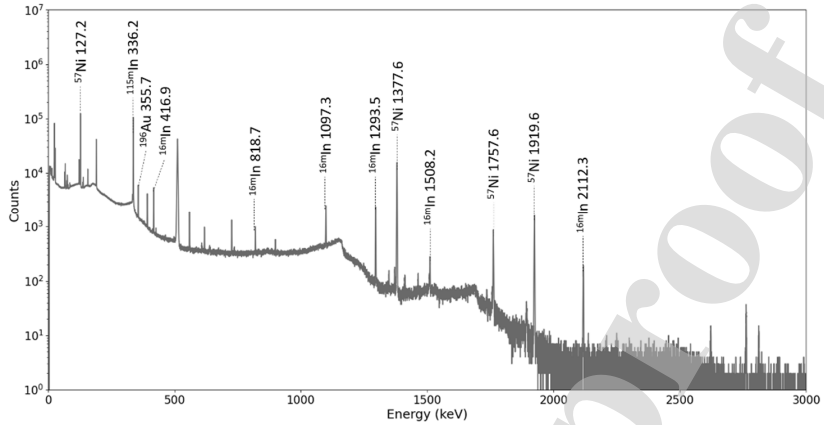

Figure 6: Activation gamma spectrum of the Au, In, Cu, Ni and Mg thin pellets

Especially, gamma rays due to (γ,n) reactions in gold and nickel isotopes were detected (see Table 3). It is worth mentioning that gold is often used as a photon flux monitor [19]-[21]. Since the characteristics of the interrogating photon beam were not known precisely, the photon activation of these materials as well as the samples themselves has been exploited in order to estimate the endpoint-energy of the bremsstrahlung beam and the corresponding photon flux. To this aim, we need to assess the electron energy distribution of the LINAC. The method we used is based on the energy-dependence of photonuclear cross-sections, and on the study of radioactive isotopes produced by these photonuclear reactions [22]. In addition to gold and nickel, ^{238}U of the depleted sample and ^{90}Zr present in both the UZr fissile core and in the Zircaloy frame of the HEU sample were also used in the spectroscopic analysis.

The characteristics of the activation products formed by (γ,n) reactions and leading to detectable gamma rays are given in Table 3. Their half-lives and gamma-ray energies are taken from JEFF-3.3 nuclear database [23]. The net areas of the gamma-ray peaks are derived from the spectra analysis with the Genie2000 software. The net area statistical uncertainty is $\sigma(N_{counts}) = \sqrt{N_{counts} + 2B}$, where B is the Compton background under the peak.

Table 3: Activation gamma rays due to the (γ,n) reaction analyzed to characterize the photon beam

Activated isotope	Activation product	Half-life	γ-ray line analyzed (keV)	Net area N_{counts}
^{197}Au	^{196}Au	6.17 days	355.8	22332 ± 589
^{58}Ni	^{57}Ni	35.9 h	127.2	427713 ± 1454
^{238}U	^{237}U	6.75 days	208.0	551097 ± 1212
^{90}Zr	^{89m}Zr	250.8 s	587.8	44363 ± 248
	^{89}Zr	3.26 days	/	/
	^{89m}Y*	15.7 s	909.0	182607 ± 438

* *From the ^{89}Zr and ^{89m}Zr decays*

Since each material has a different energy threshold and cross-section for the (γ,n) reaction, we are looking for the incident photon flux on the samples that matches the observed activation of four materials. At a distance d from the tungsten target, the experimental photon flux is given by equation (1) for gold, nickel and uranium whose gamma rays are coming from the decay of the activation product itself:

$$\Phi_{d,exp}(E_\gamma) = \frac{N_{counts}(E_\gamma) \times \lambda}{I(E_\gamma) \times \varepsilon(E_\gamma) \times f} \times \frac{1}{(1 - e^{-\lambda . t_{irr}}) \times e^{-\lambda . t_{cool}} \times (1 - e^{-\lambda . t_{count}})} \times \frac{\Phi_{d,simulated}}{\int_{E_{th}}^{E_{max}} \varphi(E) \times \sigma(E) dE} \quad (1)$$

With:

- $\Phi_{d,exp}(E_\gamma)$ the experimental integral Bremsstrahlung photon flux at a distance d, in photons.cm^{-2}.pulse^{-1} unit, calculated from the net number of counts in the peak of energy E_γ (i.e., photon flux corresponding to the measured activation in the samples);
- N_{counts} the net number of counts (after subtraction of the Compton background and of potential gamma interferences) in the gamma-ray line of interest;
- λ the radioactive decay constant of the activation product in s^{-1} from JEFF-3.3 nuclear database [23];
- $I(E_\gamma)$ the gamma-ray intensity (number of gamma ray of energy E_γ emitted per disintegration) taken from JEFF-3.3 nuclear database [23];
- $\varepsilon(E_\gamma)$ the absolute detection efficiency (number of count in the HPGe detector in the full energy peak of energy E_γ per gamma ray emitted at this energy in the sample), obtained via MCNP6.1 [24] Monte-Carlo simulation to account for the

attenuation effects in the sample, the experimental geometry (such as the distance to the detector) and the intrinsic efficiency of the detector;

- f the pulse repetition rate (or frequency) in pulse.s^{-1} (Hz);
- t_{irr}, t_{cool} and t_{count} respectively the irradiation, cooling and counting time in s;
- $\Phi_{d,simulated}$ the integral Bremsstrahlung photon flux at distance d, obtained by MCNP simulations of the LINAC accelerated electrons impacting the tungsten target, in photons.cm^{-2}.incident electron^{-1};
- $\int_{E_{th}}^{E_{max}} \varphi(E) \times \sigma(E) dE$ the number of (γ,n) reactions in the sample per incident electron, calculated with MCNP, corresponding to the Bremsstrahlung spectrum $\varphi(E)$ convolved with the reaction cross-section $\sigma(E)$, from the threshold value E_{th} of $\sigma(E)$ to the endpoint-energy E_{max} of $\varphi(E)$.

The case of ^{90}Zr is slightly different since ^{89}Zr can also be formed in an isomeric state ^{89m}Zr (587.8 keV gamma ray) following the (γ,n) reaction, and since we are also interested by the daughter nucleus ^{89m}Y (909.0 keV gamma ray) formed by both ^{89}Zr and ^{89m}Zr decays. Solving Bateman evolution equations for ^{89m}Zr, ^{89}Zr, and ^{89m}Y (simplified owing to its short half-life) enables to determine the global ^{90}Zr(γ,n) reaction rate and to calculate the flux corresponding to the observed activation of ^{90}Zr, with an equation a bit more complex than (1) but depending on the same parameters. Note that we do not take into account the pulsed emission of the LINAC in photon (or further neutron) activation equations, but we consider a continuous emission during the LINAC irradiation phase, because the half-lives of the observed nuclides are much longer than the LINAC period (0.01 s to 0.1 s).

Since we do not have the possibility to measure the electron energy distribution of our LINAC, we assume a semi-Gaussian shape based on simulations of the electron beam dynamics performed by the LINAC manufacturer [25]. In fact, we are not looking for its exact shape, but an energy distribution leading to a good agreement between measured and calculated gamma rays of the four activated materials. The semi-Gaussian function (see further Figure 7) parametrized with two variables, the endpoint-energy and the width at half-maximum, which are adjusted together. The endpoint-energy was varied from 15 MeV to 17 MeV with 0.1 MeV steps, and the width at half-maximum from 0 MeV (mono-energy distribution) to 2 MeV with 0.5 MeV steps. For each of the 105 pairs of parameters, MCNP simulations were performed by impinging electrons of the considered

energy distribution on the LINAC tungsten target to produce the Bremsstrahlung photon beam. Then, the number of (γ,n) reactions, in each activation sample was numerically evaluated, corresponding to the convolution of the resulting photon flux on the different materials with their reaction cross-section as explained above in (1). Finally, an experimental photon flux is calculated for each activated isotope (^{197}Au, ^{58}Ni, ^{238}U and ^{90}Zr) by using the net area of the peaks listed in Table 3. As a result, four photon fluxes are obtained for each couple of parameters. The most probable electron energy distribution is then identified as the one minimizing the squared differences between the four flux values. In other words, the most probable distribution among the 105 parametric cases gives the most consistent flux estimations for the four activation samples. In this case, the electron energy distribution with an endpoint-energy of 15.8 MeV and a 1 MeV width at half-maximum provides the more consistent photon fluxes for all the materials, as reported in Table 4.

Table 4: Experimental photon fluxes calculated for the four materials with the most probable electron energy distribution

Activated isotope	$\Phi_{43cm,exp}$ $(photons.cm^{-2}.pulse^{-1})$
^{197}Au	$(9.02 \pm 1.26) \times 10^7$
^{58}Ni	$(10.05 \pm 1.33) \times 10^7$
^{238}U	$(10.21 \pm 1.36) \times 10^7$
^{90}Zr	$(9.43 \pm 1.25) \times 10^7$
Mean photon flux $\bar{\phi} = (9.68 \pm 1.30) \times 10^7\ photons.cm^{-2}.pulse^{-1}$	

The uncertainty on the experimental photon flux for each material is calculated as a quadratic combination of the main following sources of uncertainty:

- a relative uncertainty estimated to 10 % on the (γ,n) cross-section of the activated isotopes, according to the EXFOR cross-section library [26]. As an example, the ^{197}Au(γ,n)^{196}Au reaction cross-section uncertainty is about 10 % in the work of Plaisir *et al.* [27];
- a relative uncertainty of 7 % on the detection efficiency to take into account the detector intrinsic efficiency (less than 5 % according to the detector model optimization with reference sources) and the modeling of the experimental set-up (uncertainties on samples and on equipment dimensions, arbitrarily set at 5 %

based on our experience of such simulations). Intrinsic and geometric efficiency uncertainties are combined in quadratic sum, leading to 7 % relative uncertainty on detection efficiency;

- the statistical uncertainty related to MCNP simulation results, which is lower than 5 % for all activation samples calculations;
- the uncertainty associated to the most probable semi-Gaussian model of the electron energy distribution is estimated as the standard deviation of the photon fluxes obtained with the four materials:

$$\frac{\sigma_{disribution}}{\bar{\phi}} = \frac{1}{\bar{\phi}}\sqrt{\frac{(\phi_{Au}-\bar{\phi})^2+(\phi_{Ni}-\bar{\phi})^2+(\phi_{U}-\bar{\phi})^2+(\phi_{Zr}-\bar{\phi})^2}{4}} = 5\ \%;$$

- the uncertainties on the radioactive decay constants of the activation products and their gamma-ray intensities, provided by JEFF-3.3 database [23], which are lower than 2 %;
- the uncertainty on the net area of the gamma rays reported in Table 3, which is at most 2.6 %.

The Bremsstrahlung beam characteristics for this most probable electron energy distribution are given in Table 5.

Table 5: Characteristics of the LINAC beam

End point energy (electron beam)	15.8 MeV
Width at half maximum (electron beam)	1 MeV
Bremsstrahlung photon flux at 43 cm from the tungsten target (0°)	$(9.68 \pm 1.30)\ 10^7\ photons.cm^{-2}.pulse^{-1}$

This electron distribution is shown in Figure 7 and the corresponding Bremsstrahlung photon distribution calculated with MCNP is given in Figure 8.

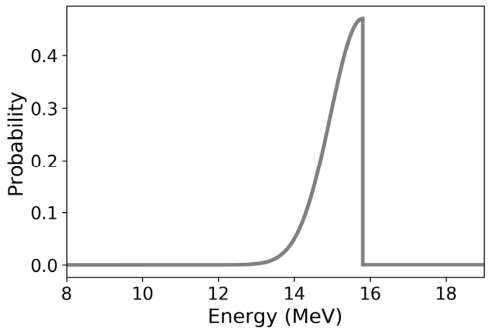

Figure 7: Most probable electron energy distribution (source of MCNP flux and reaction rate calculations)

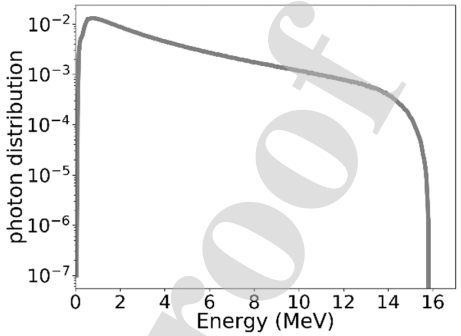

Figure 8: Bremsstrahlung photon energy distribution calculated with MCNP and the electron energy distribution of Figure 7

313

314 The mean experimental photon flux, at the center of the beam and 43 cm away from the
315 tungsten target, is used to normalize MCNP simulation results that are given per electron
316 impinging on the tungsten target.

317

318 *3.2. Neutron spectrum*

319 As mentioned in section 2, a photoneutron flux resulting from photonuclear (γ,n)
320 reactions of high-energy Bremsstrahlung photons with high-Z materials (W and Pb) is
321 expected at the location of the samples. The analysis of the pellets activation gamma
322 spectrum shown in Figure 6 spotted the presence of fast neutrons through the 336.2 keV
323 gamma-ray line of ^{115m}In, created by the ^{115}In(n,n') reaction with a threshold around 0.5
324 MeV [28]. However, this contribution is merged with that of the ^{115}In(γ,γ') reaction with a
325 poorly known cross-section. The observation of ^{116m}In gamma rays highlights the presence
326 of epithermal neutrons, i.e., with an energy larger than 0.5 MeV, which are not absorbed
327 by the cadmium foil in front of the LINAC head. On the other hand, no thermal neutrons
328 are observed through the activation of the gold foil. Indeed we do not observe the
329 411.8 keV gamma rays of ^{198}Au expected from the ^{197}Au(n,γ)^{198}Au reaction. To illustrate
330 the neutron-absorption efficiency of the LINAC head shielding, MCNP simulations of the
331 photoneutron spectrum with and without the borated polyethylene blocks and the cadmium
332 sheet in front of the collimator are shown in Figure 9. Polyethylene attenuates the fast
333 neutron flux created by photonuclear reactions on the LINAC Bremsstrahlung target and
334 on the lead collimator (76 % of photoneutrons being produced in lead), while boron and

cadmium capture thermal neutrons. However, simulations showed that cadmium leads to the production of photoneutrons in the MeV range. Altogether, the benefit of cadmium to absorb thermal neutrons causing parasitic fissions in ^{235}U is far more important than the drawback relative to the production of photoneutrons in cadmium, which are much less numerous than fast neutrons produced inside the uranium sample (see section 4.1). Finally, the global shielding decreases the neutron flux reaching the sample by a factor 4.

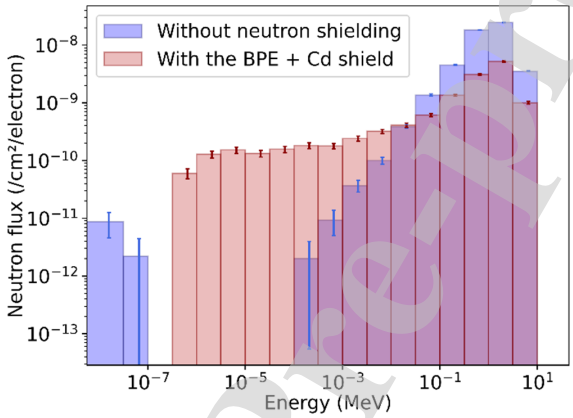

Figure 9: Simulation of the neutron energy spectrum with and without the borated polyethylene and cadmium neutron shielding around the LINAC head (tungsten target and lead collimator)

In order to validate the MCNP model, the neutron activation of indium, through the $^{115}In(n,\gamma)^{116m}In$ reaction, whose cross-section is given in Figure 10, was compared to experimental results.

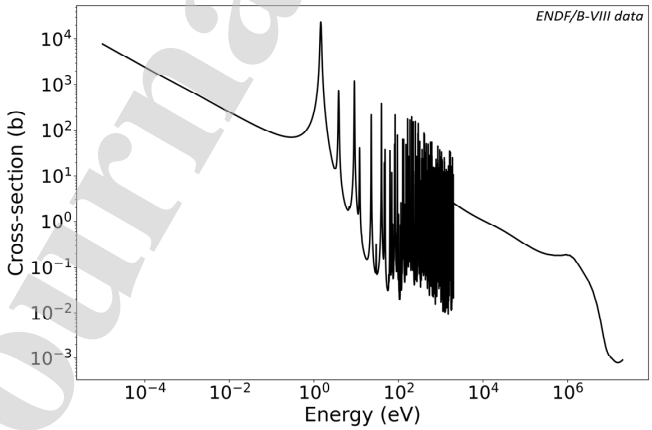

Figure 10: $^{115}In(n,\gamma)^{116m}In$ reaction cross-section, from ENDF/B-VIII.0 [17]

The net areas (number of counts) of the six ^{116m}In gamma rays visible in the spectrum of Figure 6 are compared with those calculated with MCNP6.1. The neutron spectrum of Figure 9 with the BPE and Cd shielding was simulated as a MCNP neutron source in front of the neutron Au, In, Cu, Ni and Mg activation samples. The resulting ^{115}In(n,γ)^{116m}In reaction rate in the two indium pellets enables to estimate the net surface of ^{116m}In gamma rays:

$$N(\mathrm{E_i}) = \frac{R(^{115}In(n,\gamma)^{116m}In)\ \mathrm{I(E_i)}\ \varepsilon(\mathrm{E_i})}{\lambda}\left(1-e^{-\lambda.t_{irr}}\right)e^{-\lambda.t_{cool}}\left(1-e^{-\lambda.t_{count}}\right) \qquad (2)$$

With the same notation as in (1) and with $R(^{115}In(n,\gamma)^{116m}In)$ the reaction rate in s^{-1}. The gamma-ray energies and intensities are found in JEFF-3.3 nuclear database [23]. The comparison between the simulated and the experimental numbers of counts is given in Table 6. The experimental number of counts corresponds to the peak surface calculated with Genie2000 software. The simulated number of counts is calculated with equation (2) and given with an uncertainty of 18 % corresponding to the quadratic combination of the 13.4 % uncertainty of the photon flux used to normalize the MCNP simulation result, the 7 % detection efficiency uncertainty and the 10 % uncertainty on the ^{115}In(n,γ)^{116m}In reaction cross-section. The other uncertainty sources are considered negligible.

Table 6: Experimental vs. calculated areas in the full-energy peaks of ^{116m}In gamma rays

Energy (keV)	Intensity (%)	Experiment (counts)	Simulation (counts)	Relative gap (%)
1294.5	84.7	20250 (± 287)	19101 (± 3438)	- 6
1097.3	57.6	16937 (± 373)	15463 (± 2783)	- 9
416.9	28.0	25069 (± 429)	23465 (± 4224)	- 6
2112.3	15.3	2086 (± 87)	2013 (± 362)	- 4
818.7	11.6	4756 (± 85)	4266 (± 768)	- 10
1508.2	10.4	1942 (± 52)	1994 (± 359)	+ 3

The calculated numbers of counts are globally slightly lower than the experimental ones, but the agreement is quite satisfactory taking into account the uncertainty on the calculated thermal neutron flux exiting the neutron shielding. The latter is mainly due to the uncertainty on photoneutron production (itself coming from the uncertainty on the Bremsstrahlung beam characteristics and on the (γ,n) cross-sections of W and Pb) and on the very high neutron absorption in the BPE and Cd shielding.

4. Cumulative yields of ^{235}U and ^{238}U photofission products

4.1. Estimation of neutron vs. photofission proportions

MCNP simulations were conducted to characterize neutron production inside the uranium samples via (γ,n), (n,f) and (γ,f) reactions, and their contribution to fast neutron fission (as a reminder of section 3.2, the presence of thermal neutrons was not observed), compared to photofission, which depends on sample geometry and composition of the samples, as shown in Table 7.

Table 7: Fraction of neutrons created inside the uranium samples in the total neutron flux (including photoneutrons produced outside the samples) and part of neutron fissions (in all fissions including photofissions)

	DU	**HEU**
Part of neutrons produced inside the sample (%)	99	66
Part of neutron fissions among total fissions (%)	5.5	0.5

For the thick Depleted Uranium (DU) sample, simulations show that neutrons produced inside the sample itself represent 99 % of the total neutron flux in the sample. They are mainly produced via (γ,n) and (γ,2n) reactions, or during photofissions, and they induce fast neutron fissions representing 5.5 % of total fissions. For the Highly Enriched Uranium (HEU) sample, 66 % of the neutrons are created in the sample itself. Among them, 30 % are produced by (γ,xn) reactions on zirconium isotopes of the UZr fissile core and its Zircaloy support. For this HEU sample, fast neutron fissions only represent 0.5 % of total fissions because of the small thickness of the sample (neutron escape without interaction). It can be noted that photoneutron production outside uranium samples (mainly in the LINAC tungsten target and lead collimator) has no significant impact on the parasitic neutron fission rate for this experimental configuration.

For the purpose of calculating the photofission product yields, the photofission rate in the samples is calculated with MCNP. It significantly depends on the sample geometry and density because of self-shielding, i.e. attenuation of the Bremsstrahlung photon flux inside the sample. The validity of the DU sample numerical model was first verified by comparing the experimental and simulated (γ,n) reaction rates on ^{238}U, forming ^{237}U that emits a 208.0 keV gamma ray following its β^- decay. Given the relatively long half-life of

^{237}U (almost 7 days) with respect to the irradiation time (2 hours), the experimental reaction rate can be calculated with (3) using the net area of the 208.0 keV peak.

$$R_{exp}\left[^{238}U(\gamma,n)^{237}U\right] = \frac{N_{counts}(208\ \text{keV})}{\text{I}(208\ \text{keV}) \times \varepsilon(208\ \text{keV}) \times \text{e}^{-\lambda.t_{cool}} \times (1 - \text{e}^{-\lambda.t_{count}}) \times t_{irr} \times f} \quad (3)$$

With the same notation as in (1) and with $R_{exp}\left[^{238}U(\gamma,n)^{237}U\right]$ the experimental reaction rate per LINAC pulse. The uncertainty on $R_{exp}\left[^{238}U(\gamma,n)^{237}U\right]$ is estimated as the quadratic combination of 7 % relative uncertainty on the detection efficiency (quadratic combination of 5 % uncertainties on both the detector intrinsic efficiency and geometric efficiency), 0.3 % uncertainty on the 208.0 keV gamma-ray intensity (JEFF-3.3 database [23]), and 0.22 % statistical uncertainty on the 208.0 keV gamma-ray net area (see Table 3). Finally, we obtain $R_{exp}\left[^{238}U(\gamma,n)^{237}U\right] = (7.51 \pm 0.53) \times 10^5\ reactions.pulse^{-1}$.

For comparison, the reaction rate can be calculated with MCNP model as in (4):

$$R_{simul}\left[^{238}U(\gamma,n)^{237}U\right] = \int_{E_{th}}^{E_{max}} \varphi(E) \times \sigma_{(\gamma,n)}(E)\, dE \times \frac{\Phi_{exp}}{\Phi_{simulated}} \quad (4)$$

With:

- $R_{simul}\left[^{238}U(\gamma,n)^{237}U\right]$ the simulated reaction rate per LINAC pulse;
- $\int_{E_{th}}^{E_{max}} \varphi(E) \times \sigma_{(\gamma,n)}(E)\, dE$ the number of (γ,n) reactions in the DU sample per source electron, calculated with MCNP, corresponding to the Bremsstrahlung spectrum $\varphi(E)$ convolved with the (γ,n) reaction cross-section $\sigma_{(\gamma,n)}(E)$, from the threshold value E_{th} of $\sigma_{(\gamma,n)}(E)$ to the endpoint-energy E_{max} of $\varphi(E)$;
- Φ_{exp} the integral Bremsstrahlung photon flux in front of the DU sample reported in section 3.1 (photon activation measurements with four material targets): $(9.68 \pm 1.30) \times 10^7\ photons.cm^{-2}.pulse^{-1}$;
- $\Phi_{simulated}$ the integral Bremsstrahlung photon flux in front of the DU sample, obtained by MCNP simulations of LINAC accelerated electrons impacting the tungsten target, in photons.cm^{-2}.source electron^{-1}.
- Note that the term $\frac{\Phi_{exp}}{\Phi_{simulated}}$ provides the number of source electrons per LINAC pulse, necessary to normalize the MCNP simulation result of the reaction rate $\int_{E_{min}}^{E_{max}} \varphi(E) \times \sigma_{(\gamma,n)}(E)\, dE$ (in reactions per source electron).

The uncertainty on $R_{simul}[^{238}U(\gamma,n)^{237}U]$ is calculated as the quadratic combination of the 13.4 % relative uncertainty on Φ_{exp} as reported in section 3.1, the 10 % uncertainty on the ^{238}U(γ,n)^{237}U cross-section in accordance with the EXFOR library [26], and the 0.4 % statistical uncertainty on the Monte-Carlo calculation for the ^{238}U(γ,n)^{237}U reaction rate. Finally, we obtain $R_{simul}[^{238}U(\gamma,n)^{237}U] = (7.15 \pm 1.19) \times 10^5\ reactions.pulse^{-1}$.

We obtain a satisfactory agreement between the experimental and simulated ^{238}U(γ,n)^{237}U reaction rates per LINAC pulse, which worth respectively $(7.51 \pm 0.53) \times 10^5$ and $(7.15 \pm 1.19) \times 10^5$, reinforcing our confidence in the numerical model of the DU sample and in the Bremsstrahlung photon beam determined in section 3.1. Consequently, we can simulate the photofission rate in the samples, defined by (5) for a mixture of ^{235}U and ^{238}U.

$$\tau_p = \frac{N_A}{\mathcal{M}}\left(m_5 \int_{E_{th}}^{E_{max}} \varphi(E)\sigma_{5(\gamma,f)}(E)dE + m_8 \int_{E_{th}}^{E_{max}} \varphi(E)\sigma_{8(\gamma,f)}(E)dE\right) \quad (5)$$

Where:

- τ_p is the photofission rate in s^{-1};
- N_A is the Avogadro constant, equal to $6.02 \times 10^{23}\ mol^{-1}$;
- $\mathcal{M}$ is the molar mass of the uranium mixture, expressed in g.mol^{-1};
- m_5 and m_8 are respectively the ^{235}U and ^{238}U masses in the sample, in g;
- E_{th} and E_{max} are respectively the threshold energy of the photofission reactions, around 6 MeV, and the Bremsstrahlung endpoint-energy, 15.8 MeV in this case;
- $\varphi(E)$ is the Bremsstrahlung photon flux at the energy E in the sample;
- $\sigma_{5(\gamma,f)}(E)$ and $\sigma_{8(\gamma,f)}(E)$ are the photofission reaction cross-sections at the energy E for ^{235}U and ^{238}U, respectively.

The uncertainty on the photofission rate calculated with MCNP is the quadratic combination of the following uncertainties:

- 13.4 % relative uncertainty on the bremsstrahlung photon flux, determined in section 3.1, $(9.68 \pm 1.30) \times 10^7\ photons.cm^{-2}.pulse^{-1}$ (see Table 5);
- 0.4 % and 0.8 % relative statistical uncertainties on MCNP calculations for the photofission rate in the DU and HEU samples, respectively;
- 2 % uncertainty on the photofission cross-section, according to datasets available in the EXFOR library [26];

- 2 % uncertainty on the uranium mass of the HEU sample, and a negligible uncertainty (smaller than 1 %) on the uranium mass of the DU sample.

Finally, using the characteristics of the beam (electron energy distribution and photon flux) and the experimental position of the samples with respect to the tungsten target, the photofission rates in the samples calculated with MCNP are:

$$\tau_{p,DU} = (2.80 \pm 0.38) . 10^{6}\ s^{-1}$$

$$\tau_{p,HEU} = (1.04 \pm 0.14) . 10^{5}\ s^{-1}$$

Given the 0.3 % ^{235}U content of the DU sample, we consider that all fissions occur on ^{238}U. As a result, the delayed gamma rays measured with the DU sample are used to directly calculate the ^{238}U photofission products cumulative yields. In the HEU sample, however, 3.7 % of photofissions occur on ^{238}U nuclei and 96.3 % on ^{235}U nuclei. Therefore, the ^{238}U contribution to photofission will be subtracted to calculate the ^{235}U photofission products cumulative yields.

4.2. Photofission product yields computation

Figures 11 to 13 show the delayed gamma spectrum of the DU sample recorded during 67 h, after a 2 h irradiation and a 30 s cooling time. The notations used are PE for Passive Emission, AP for Activation Product and FP for Fission Product.

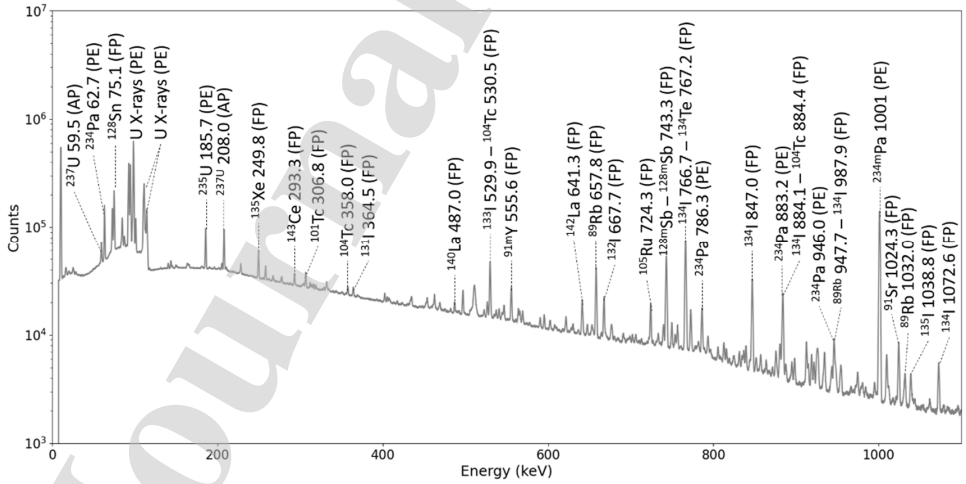

Figure 11: Delayed gamma spectrum of the DU sample (0-1100 keV) recorded during 67 h, after a 2 h irradiation and a 30 s cooling time

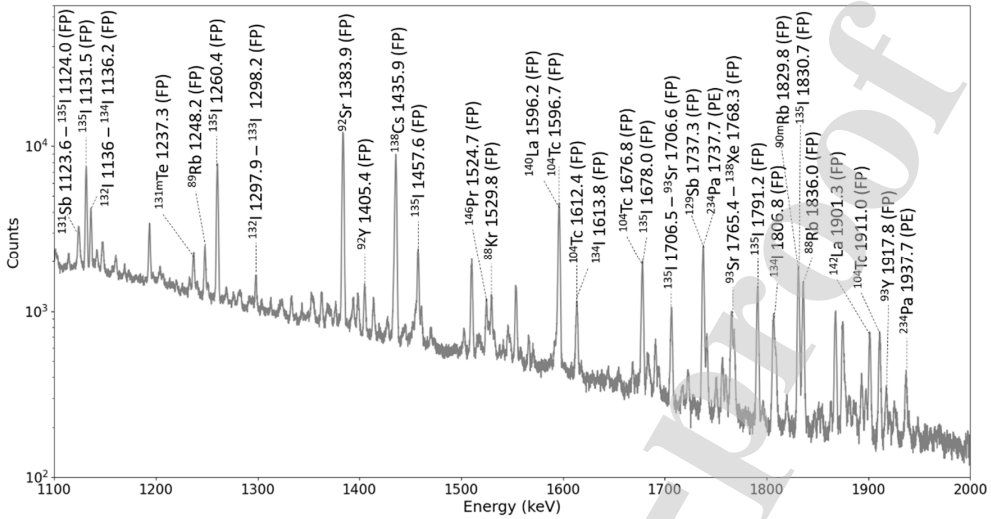

Figure 12: Delayed gamma spectrum of the DU sample (1100-2000 keV) recorded during 67 h, after a 2 h irradiation and a 30 s cooling time

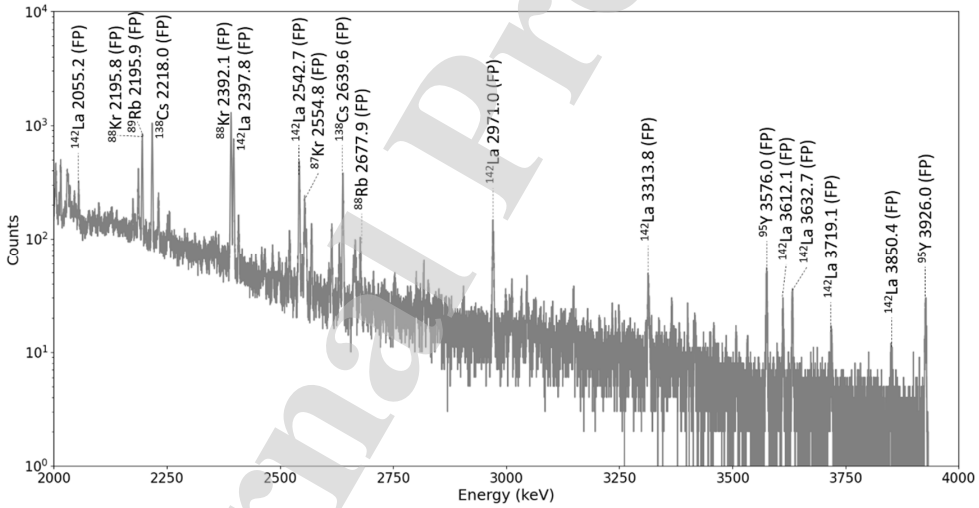

Figure 13: Delayed gamma spectrum of the DU sample (2000-4000 keV) recorded during 67 h, after a 2 h irradiation and a 30 s cooling time

Figures 14 to 16 show the delayed gamma spectrum of the HEU sample recorded during 22 h, after a 2 h irradiation and a 30 s cooling time. The notations are the same as those for Figures 11 to 13.

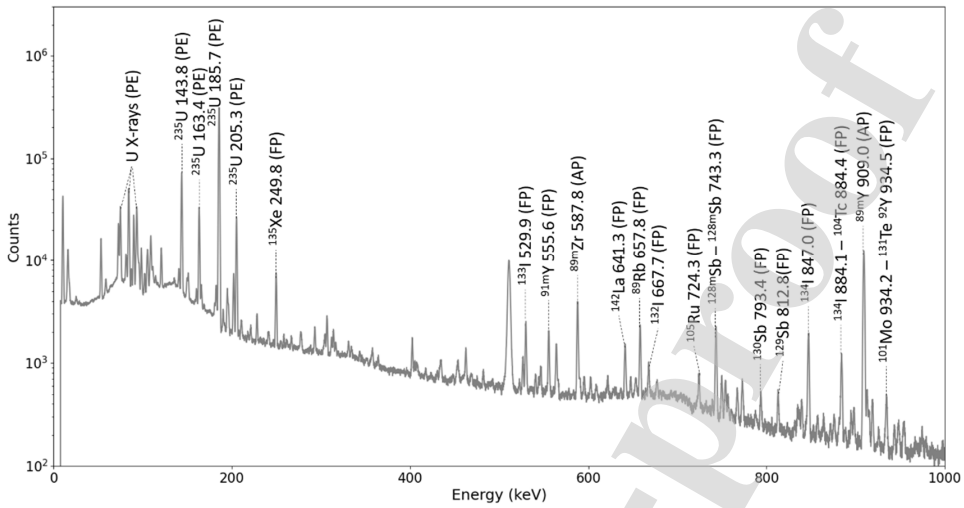

488

489 *Figure 14: Delayed gamma spectrum of the HEU sample (0-1000 keV) recorded during 22 h, after a 2 h irradiation and*
490 *a 30 s cooling time*

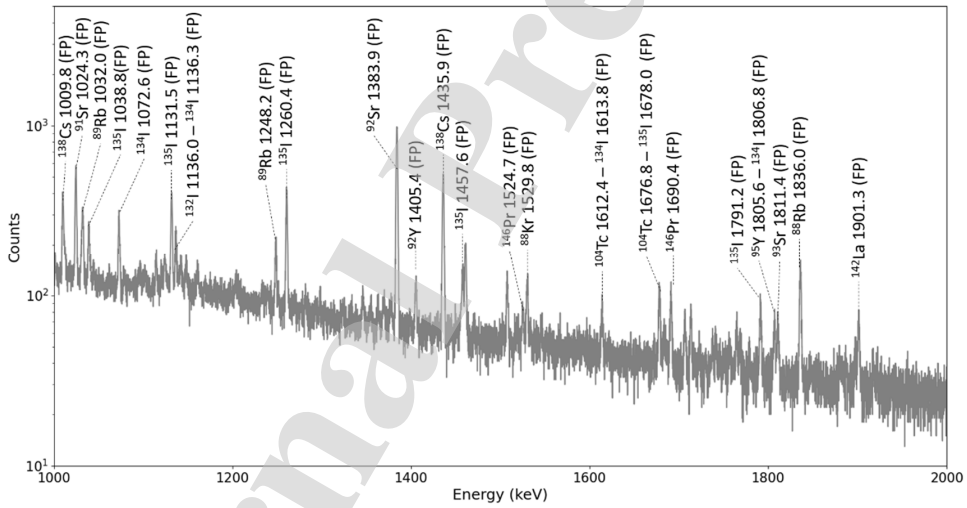

491

492 *Figure 15: Delayed gamma spectrum of the HEU sample (1000-2000 keV) recorded during 22 h, after a 2 h irradiation*
493 *and a 30 s cooling time*

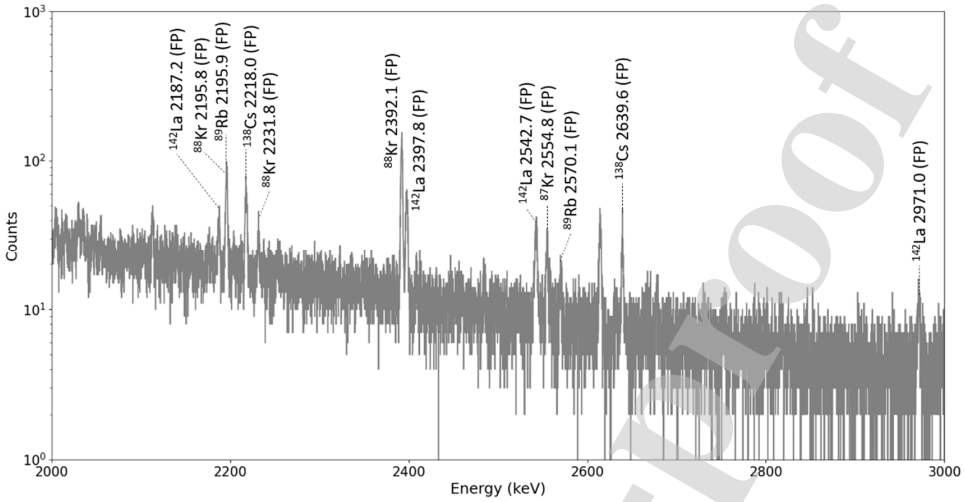

Figure 16: Delayed gamma spectrum of the HEU sample (2000-3000 keV) recorded during 22 h, after a 2 h irradiation and a 30 s cooling time

For the DU sample, the delayed gamma-ray spectra have been recorded by sequences of 60 s during the almost three days of acquisition, which allows a spectrum analysis with different cooling and measurement times to limit some interferences between gamma rays close in energy, by exploiting the period differences of their emitting isotopes. For the HEU sample, the acquisition sequences lasted 180 s and the total counting time almost one day. The spectra analysis is performed with the MAGIX code developed by CEA LIST, in collaboration with CEA DES to analyze complex gamma- and X-ray spectra measured with HPGe detectors. This automatic software, based on CEA LIST know-how in complex spectrum processing [29][30], performs a complete analysis of the spectrum: energy calibration, identification of radionuclides, peak deconvolution, determination of a relative detection efficiency, activity calculation for each radionuclide if the absolute efficiency is provided by the end-user, and otherwise activity ratios. One of its main features is to include iterative steps with the automatic analysis of gamma- and X-rays JEFF-3.3 database [23] in order to identify all the peaks associated to the radionuclides potentially present in the list provided by the user.

Theoretically speaking, the fission products created during the irradiation are part of radioactive decay chains and their activities can be calculated by solving Bateman

equations [31]. In general, these equations can be simplified by considering only the activation of the photofission product emitting the delayed gamma rays of interest, as below in (6). However, as explained further to introduce (7), we sometimes also need to consider the direct precursor of the photofission product of interest which are respectively called the father and daughter nuclides, like in the work of Kahane *et al.* [5] and Carrel *et al.* [6].

When the delayed gamma rays are emitted by a nucleus with a much longer half-life than its precursors and the cooling time, the net area $N(E_i)$ of its gamma rays of energy E_i is directly related to ^{235}U and ^{238}U cumulative photofission yields $Y_{c5,p}$ and $Y_{c8,p}$ through equation (6):

$$N(E_i) = \frac{I(E_i)\,\varepsilon(E_i)}{\lambda_j}\left(1 - e^{-\lambda.t_{irr}}\right)e^{-\lambda.t_{cool}}\left(1 - e^{-\lambda.t_{count}}\right)\left[\tau_p\left(\eta_{8,p}Y_{c8,p} + \eta_{5,p}Y_{c5,p}\right) + \tau_n\left(\eta_{8,n}Y_{c8,n} + \eta_{5,n}Y_{c5,n}\right)\right] \quad (6)$$

With the same notations as in (1) and (2), and:

- $\varepsilon(E_i)$ the absolute detection efficiency taking into account, in addition to the abovementioned intrinsic detector and geometric efficiencies, the interrogating photon flux self-shielding and delayed gamma self-attenuation in the uranium sample, both estimated with MCNP. For example, regarding the self-shielding in the DU sample, the photofission rate is 2.5 times higher on the entrance surface of the sample, with respect to the LINAC photon beam, than on its rear exit surface. Concerning self-attenuation, for instance, less than 60 % of 1 MeV delayed gamma rays emitted in the DU sample manage can escape from it;
- λ_j the radioactive decay constant of the fission product j in s^{-1};
- τ_p and τ_n the photofission and neutron fission rates in the sample, in s^{-1};
- $Y_{c5,p}$ and $Y_{c8,p}$ the cumulative photofission yields of photofission product j, respectively for ^{235}U and ^{238}U;
- $Y_{c5,n}$ and $Y_{c8,n}$ the cumulative fast neutron fission product yields of fission product j, respectively for ^{235}U and ^{238}U, taken from JENDL database [32];
- $\eta_{5,p}$ and $\eta_{8,p}$ are the fractions of photofissions occurring respectively in ^{235}U and ^{238}U, determined via MCNP simulation;
- $\eta_{5,n}$ and $\eta_{8,n}$ are the fractions of neutron fissions occurring respectively in ^{235}U and ^{238}U, determined via MCNP simulations.

However, when the photofission product of interest is a daughter nuclide in a decay chain with a father having a similar half-life (for instance ^{134}I and ^{138}Cs, which are respectively the daughters of ^{134}Te and ^{138}Xe, see radioactive periods in Table 8), its net peak areas are given by (7).

$$N(E_i) = I(E_i)\varepsilon(E_i)(\tau_p[\eta_{8,p}(Y^d_{i8,p}f_d + Y^f_{c8,p}f_f) + \eta_{5,p}(Y^d_{i5,p}f_d + Y^f_{c5,p}f_f)] \ldots + \tau_n[\eta_{8,n}(Y^d_{i8,n}f_d + Y^f_{c8,n}f_f) + \eta_{5,n}(Y^d_{i5,n}f_d + Y^f_{c5,n}f_f)]) \quad (7)$$

Where:

- $I(E_i)$, $\varepsilon(E_i)$, τ_p, τ_n, $\eta_{8,p}$, $\eta_{5,p}$, $\eta_{8,n}$ and $\eta_{5,n}$ keep the same meaning as in (6);
- $Y^f_{c5,p}$ and $Y^f_{c8,p}$ are the cumulative yields of the father nuclide, respectively for the photofission of ^{235}U and ^{238}U;
- $Y^d_{i5,p}$ and $Y^d_{i8,p}$ are the independent yields of the daughter nuclide, respectively for the photofission of ^{235}U and ^{238}U. The independent yield (in %) of a photofission product corresponds to the number of nuclei created per 100 photofissions of the considered actinide, right after the prompt neutron emission but before the delayed neutron emission. These values will be calculated to determine the cumulative photofission yield of the daughter nuclide, which is the sum of its independent yield together with that of its precursor. Note that as in Kahane *et al.* [5] and Carrel *et al.* [6], we only consider one precursor since the precursors of the father nuclide have a relatively short half-life compared to the cooling time of these experiments. In this case, we can write $Y^d_{c,p} = Y^d_{i,p} + Y^f_{c,p}$
- $Y^f_{c5,n}$ and $Y^f_{c8,n}$ are the cumulative yields of the father nuclide, respectively for the neutron fission of ^{235}U and ^{238}U. These values are taken from JENDL database [32];
- $Y^d_{i5,n}$ and $Y^d_{i8,n}$ are the independent yields of the daughter nuclide, respectively for the neutron fission of ^{235}U and ^{238}U. These values are taken from JENDL database [32];
- The terms f_d and f_f describe the evolution of the number of nuclei over time, and are given by:

$$f_d = \frac{1}{\lambda_d}\left(1 - e^{-\lambda_d . t_{irr}}\right) e^{-\lambda_d . t_{cool}} \left(1 - e^{-\lambda_d . t_{count}}\right)$$

$$f_f = \frac{1}{\lambda_d - \lambda_f}\left[\frac{\lambda_d}{\lambda_f}\left(1 - e^{-\lambda_f . t_{irr}}\right) e^{-\lambda_f . t_{cool}} \left(1 - e^{-\lambda_f . t_{count}}\right) \ldots \right.$$
$$\left. \ldots - \frac{\lambda_f}{\lambda_d}\left(1 - e^{-\lambda_d . t_{irr}}\right) e^{-\lambda_d . t_{cool}} \left(1 - e^{-\lambda_d . t_{count}}\right)\right]$$

With λ_d and λ_f the radioactive decay constants of the daughter and father nuclides (in s^{-1}), respectively, and t_{irr}, t_{cool}, t_{count} the irradiation, cooling and counting times (in s).

Note that when the father nuclide half-life is much shorter than that of the daughter nuclide, the cumulative yield of the daughter nuclide can be estimated with (6) by analyzing the delayed gamma spectrum after a cooling time equal to six times the half-life of the father nuclide (corresponding to the decay of 98.5 % of father nuclei). This approach is used in practice for the majority of fission products, the precursors of which having very short half-lives. However, in some instances, the half-life of the precursor is a few minutes, or dozen minutes, and this approach requires that a sufficient number of daughter nuclei are still present after the abovementioned cooling time, so that their delayed gamma rays can be counted with sufficient statistics. On the contrary, when the daughter nuclide half-life is very short compared to that of the father nuclide, (6) can be used to determine the independent yield of the daughter nuclide instead of its cumulative yield.

Concerning the DU sample enrichment of only 0.3 % (^{238}U), the measured delayed gamma rays directly lead to the photofission products cumulative yields of ^{238}U. However, according to Table 7, neutron fissions on ^{238}U represent 5.5 % of total fissions in the sample. Therefore, we use the ^{238}U fast neutron fission yields available in JENDL database [32] to subtract the neutron fission contribution to the net areas of the gamma rays emitted by the fission products created in this sample. For the HEU sample, the neutron fissions represent only 0.5 % among total fissions, so we decided to neglect this contribution, but we subtract the 3.7 % of photofissions in ^{238}U nuclei present in the HEU sample to calculate the ^{235}U photofission products cumulative yields. For this purpose, we use the photofission yields obtained in this work for ^{238}U to evaluate the ^{235}U yields.

Finally, 26 and 49 photofission products have been identified in the spectra from their delayed gamma rays, respectively for ^{235}U and ^{238}U, and their cumulative photofission yields calculated from (6) or (7). The cumulative photofission yields measured for ^{238}U and ^{235}U are given respectively in Table 8 and Table 10 under the denomination "This work". Note that when several delayed gamma rays are measured for a photofission product, we calculate a weighted average of the cumulative yields obtained with all the peaks that are correctly processed by MAGIX software (outliers of the net areas, for instance due to interferences, are discarded). The weighting coefficient for each gamma ray is defined as the inverse of the squared relative uncertainty on the net peak area, as described in (8):

$$\overline{y_c} = \frac{\sum_{i=1}^{N} \frac{y_{c,i}(E_i)}{\left(\frac{\sigma(N(E_i))}{N(E_i)}\right)^2}}{\sum_{i=1}^{N} \frac{1}{\left(\frac{\sigma(N(E_i))}{N(E_i)}\right)^2}} \quad (8)$$

Where $y_{c,i}(E_i)$ is the cumulative photofission yield calculated with the net peak area $N(E_i)$ of the gamma ray of energy E_i, and $\sigma(N(E_i))$ is the statistical uncertainty calculated by $\sigma(N(E_i)) = \sqrt{N(E_i) + 2B}$, B being the Compton background under this peak.

The uncertainty associated to the average cumulative yield is calculated with a quadratic propagation of the main uncertainties listed below:

- the uncertainty on the photofission rate in the samples, respectively 13.6 % for the DU sample and 13.4 % for the HEU sample (refer to section 4.1). This uncertainty is the largest one and mainly comes from the uncertainty on the interrogating Bremsstrahlung photon flux. It could be reduced by accurately measuring the (γ,n) cross-sections of the activation materials used to characterize the photon beam, since their current uncertainties are around 10 % in EXFOR library [26];
- the uncertainty on the absolute detection efficiency of the gamma ray of energy E_i, which is estimated to 7 %;

- the relative statistical uncertainty on the weighted average (8), $\frac{\sigma_{stat}(\overline{y_c})}{\overline{y_c}}$, with $\sigma_{stat}(\overline{y_c}) = \sqrt{\frac{1}{\sum_{i=1}^{N}\left(\frac{N(E_i)}{\sigma(N(E_i))}\right)^2}}$.

We provide in Table 9 and Table 11 all the details of the delayed gamma-ray analysis for ^{238}U and ^{235}U, respectively: cooling and counting times for each delayed gamma ray, energy and intensity coming from JEFF-3.3 database [23]**Error! Reference source not found.**, net peak area with its associated uncertainty and cumulative yield computed for each line.

Our work is then compared to the values of photofission products cumulative yields previously published. Note that we report a simple average of the yields when several gamma rays are given in the other publications. The characteristics of the interrogating photon beams are indicated in the first two lines of Table 8 and Table 10. For Bremsstrahlung photon beams, the energy indicated corresponds to the endpoint energy. The nuclides half-lives are from JEFF-3.3 database [23], except for ^{92}Sr because it is not consistent in the different databases, and therefore its half-life is taken from Leconte *et al.* [33].

Table 8: Cumulative yields (number of photofission product per 100 fissions) for the photofission of ^{238}U and comparison with published data

Photon beam type		Bremsstrahlung	Neutron-capture gamma rays	Bremsstrahlung	Bremsstrahlung	Bremsstrahlung	Bremsstrahlung	Bremsstrahlung	Monoenergetic
Energy (MeV)		15.8	7.8	16.3	10.0	14.987	8.0	22.0	13.0
Fission Product	**$T_{1/2}$**	**This work**	**Kahane 1985 [5]**	**Carrel 2011 [6]**	**Naik 2011 [7]**	**Naik 2013 [8]**	**Naik 2014 [9]**	**Wen 2016 [10]**	**Krishichayan 2019 [11]**
^{84}Br	31.8 min	1.37 ± 0.20	-	-	-	0.90 ± 0.06	0.30 ± 0.06	-	2.49 ± 0.19
^{87}Kr	1.3 h	1.96 ± 0.31	1.82 ± 0.21	-	1.61 ± 0.20	1.86 ± 0.30	1.11 ± 0.13	1.0 ± 0.06	2.29 ± 0.16
^{88}Kr	2.8 h	2.24 ± 0.34	-	2.52 ± 0.23	2.77 ± 0.53	2.58 ± 0.19	2.77 ± 0.38	1.0 ± 0.03	2.92 ± 0.17
^{88}Rb	17.8 min	2.68 ± 0.79	-	2.82 ± 0.19	-	-	-	-	-
^{89}Rb	15.4 min	3.50 ± 0.55	2.51 ± 0.40	3.30 ± 0.20	-	3.12 ± 0.16	3.42 ± 0.34	1.4 ± 0.13	-
^{90}Rb	2.6 min	1.67 ± 0.27	-	-	-	-	-	-	-
^{90m}Rb	4.3 min	1.06 ± 0.17	-	-	-	-	-	-	-
^{91}Sr	9.7 h	3.86 ± 0.60	3.81 ± 0.45	4.53 ± 0.22	3.82 ± 0.17	3.69 ± 0.23	4.75 ± 0.48	-	5.27 ± 0.18
^{91m}Y	49.7 min	2.35 ± 0.49	3.84 ± 0.44	4.43 ± 0.21	-	-	-	-	-
^{92}Sr	2.6 h	4.04 ± 0.63	-	4.77 ± 0.22	3.83 ± 0.45	4.26 ± 0.13	4.59 ± 0.47	1.7 ± 0.02	4.82 ± 0.15
^{92}Y	3.5 h	4.79 ± 0.81	4.16 ± 0.21	-	-	-	-	-	8.48 ± 0.96
^{93}Sr	7.4 min	4.44 ± 0.84	-	4.90 ± 0.23	-	-	-	-	-
^{93}Y	10.2 h	4.70 ± 0.94	-	-	5.47 ± 0.76	4.00 ± 0.21	3.91 ± 0.40	-	9.53 ± 1.45
^{94}Sr	1.3 min	4.35 ± 0.68	-	4.97 ± 0.23	-	-	-	-	-

^{94}Y	18.7 min	4.48 ± 0.77	-	5.06 ± 0.24	-	4.47 ± 0.25	4.25 ± 0.47	-	7.50 ± 0.46
^{95}Y	10.3 min	4.85 ± 0.72	-	5.84 ± 0.39	-	-	6.20 ± 0.69	-	-
^{97}Zr	16.7 h	5.95 ± 0.93	5.89 ± 0.66	-	5.43 ± 0.19	5.78 ± 0.17	6.00 ± 0.64	-	6.20 ± 0.19
^{99}Mo	2.7 d	4.65 ± 0.77	-	-	4.84 ± 0.44	5.11 ± 0.15	4.75 ± 0.50	-	6.57 ± 0.22
^{99m}Tc	6 h	4.36 ± 0.70	-	-	-	-	-	-	-
^{101}Mo	14.6 min	5.37 ± 0.86	-	6.78 ± 0.32	-	7.13 ± 0.30	7.56 ± 0.77	-	-
^{101}Tc	14.2 min	5.61 ± 1.20	6.98 ± 0.82	-	-	-	-	-	-
^{104}Tc	18.3 min	3.60 ± 0.56	4.13 ± 0.50	-	-	3.65 ± 0.28	4.06 ± 0.42	-	4.44 ± 0.64
^{105}Ru	4.4 h	2.76 ± 0.44	2.95 ± 0.45	-	2.57 ± 0.21	2.55 ± 0.06	2.91 ± 0.38	-	4.06 ± 0.20
^{105}Rh	1.5 d	2.78 ± 0.49	2.85 ± 0.38	-	2.63 ± 0.28	2.58 ± 0.05	2.98 ± 0.40	-	3.42 ± 0.11
^{128}Sn	59.1 min	0.57 ± 0.09	-	-	-	0.85 ± 0.04	0.21 ± 0.03	-	1.22 ± 0.22
^{128}Sb	9 h	0.21 ± 0.03	-	0.16 ± 0.01	-	-	-	-	-
^{128m}Sb	10.4 min	1.73 ± 0.25	-	-	-	-	-	-	-
^{129}Sb	4.4 h	1.09 ± 0.17	0.54 ± 0.10	1.33 ± 0.06	1.48 ± 0.33	1.35 ± 0.16	0.63 ± 0.06	-	2.59 ± 0.09
^{130}Sn	3.7 min	0.47 ± 0.10	-	-	-	-	-	-	-
^{130}Sb	39.5 min	0.79 ± 0.12	-	1.08 ± 0.05	-	-	-	-	1.61 ± 0.11
^{131}Sb	23 min	2.51 ± 0.37	-	3.94 ± 0.19	-	4.18 ± 0.18	2.40 ± 0.27	-	5.01 ± 0.33
^{131m}Te	1.3 d	0.70 ± 0.10	3.12 ± 0.40	-	-	-	-	-	-
^{132}Te	3.2 d	4.71 ± 0.73	2.43 ± 0.50	-	4.84 ± 0.46	5.48 ± 0.14	6.15 ± 0.65	-	5.44 ± 0.25
^{132}I	2.3 h	4.87 ± 0.76	3.74 ± 0.46	-	-	-	-	-	-
^{133}Sb	2.5 min	2.59 ± 0.42	-	-	-	-	-	-	-
^{133m}Te	55.4 min	3.23 ± 0.44	2.35 ± 0.39	4.43 ± 0.21	-	-	-	3.8 ± 0.42	-
^{134}Te	41.8 min	5.29 ± 0.84	6.25 ± 0.89	6.34 ± 0.30	8.27 ± 0.26	7.23 ± 0.33	7.21 ± 0.74	-	7.43 ± 0.51
^{134}I	52.5 min	7.30 ± 1.16	6.29 ± 0.94	-	-	8.06 ± 0.34	8.63 ± 0.87	3.1 ± 0.19	-
^{135}I	6.6 h	5.85 ± 0.92	5.91 ± 0.68	6.66 ± 0.42	5.88 ± 0.57	5.57 ± 0.12	6.55 ± 0.67	2.6 ± 0.16	6.13 ± 0.29
^{135m}Xe	15.3 min	1.32 ± 0.43	-	-	-	-	-	-	-
^{138}Xe	14.1 min	3.75 ± 0.59	5.38 ± 0.90	6.60 ± 0.58	-	-	5.91 ± 0.63	1.8 ± 0.41	-
^{138}Cs	33.4 min	5.91 ± 0.86	6.10 ± 0.71	-	8.00 ± 0.48	6.84 ± 0.25	6.44 ± 0.68	2.6 ± 0.10	-
^{140}Cs	64 s	5.65 ± 0.92	-	-	-	-	-	-	
^{140}La[(a)]	1.7 d	5.72 ± 0.92	-	-	-	-	-	-	-
^{141}Ba	18.3 min	4.75 ± 0.73	-	-	-	4.51 ± 0.23	5.44 ± 0.56	-	-
^{142}Ba	10.6 min	4.38 ± 0.78	-	4.66 ± 0.22	-	4.38 ± 0.29	4.68 ± 0.50	-	-
^{142}La	1.5 h	4.89 ± 0.88	3.69 ± 0.43	5.01 ± 0.24	5.26 ± 0.52	4.69 ± 0.20	4.88 ± 0.52	1.7 ± 0.13	5.58 ± 0.18
^{143}Ce	1.4 d	4.39 ± 0.68	5.38 ± 0.62	-	4.27 ± 0.29	4.74 ± 0.14	4.73 ± 0.53	-	4.92 ± 0.15
^{146}Pr	24.2 min	5.89 ± 0.91	3.24 ± 0.44	-	-	3.08 ± 0.17	3.27 ± 0.36	-	-

[(a)] The cumulative yield of ^{140}Ba could not have been calculated considering its long half-life of almost 13 days (compared to the counting time of less than 3 days). We assume that the independent photofission yield of ^{140}Ba is negligible, as it is the case for neutron fission ($Y_{i,8}(^{140}Ba) = 0.027$ % according to JENDL database [32]). Since the half-life of ^{140}La is much shorter than that of its father nuclide ^{140}Ba (1.7 days vs. 13 days), the independent yield of ^{140}La can be calculated by analyzing the delayed gamma spectrum. We assume that the sum of the ^{140}Cs cumulative yield and the ^{140}La independent yield provide a relevant estimation of the ^{140}La cumulative yield.

644 *Table 9: Detailed data of the delayed gamma-ray analysis for each ^{238}U photofission product*

Fission Product	Cooling time (s)	Counting time (s)	Gamma-ray energy (keV)	Relative intensity (%)	Net peak area (counts)	Photofission cumulative yield (%)
^{84}Br	1185	11429	881.60	41.60	9965 ± 174	1.37
^{87}Kr	334	27474	402.59	49.60	42830 ± 403	1.99
			2554.80	9.23	3882 ± 70	1.87
			2558.10	3.92	1646 ± 52	1.87
			2011.88	2.88	1497 ± 78	2.01
^{88}Kr	30	61362	2392.11	34.60	24501 ± 164	2.18
			834.83	12.97	18760 ± 287	2.34
			196.30	25.98	17385 ± 582	2.34
			1529.77	10.93	11463 ± 156	2.27
			2029.84	4.53	3860 ± 98	2.46
			2035.41	3.74	3441 ± 96	2.46
			2231.77	3.39	2658 ± 78	2.26
^{88}Rb	30	67713	1836.02	22.40	23215 ± 173	2.68
^{89}Rb	1003	6626	1032.00	63.60	14361 ± 159	3.55
			1248.20	45.60	9090 ± 129	3.42
			657.80	11.00	2723 ± 185	3.42
^{90}Rb	30	912	831.68	39.90	1665 ± 103	1.62
			3383.4	6.66	109 ± 15	1.90
^{90m}Rb	213	1519	831.69	94.09	2228 ± 114	1.06
^{91}Sr	334	208128	1024.30	33.50	88784 ± 381	3.89
			749.80	23.68	67494 ± 485	3.77
			652.90	8.04	24203 ± 478	3.89
^{91m}Y	30	226302	555.57	95.00	179440 ± 688	2.35
^{92}Sr	30	61362	1383.90	93.00	185418 ± 450	4.05
					6065 ± 195	3.86
^{92}Y	30	134990	561.10	2.39	9197 ± 466	4.79
^{93}Sr	30	3829	1387.11	3.47	843 ± 87	4.44
^{93}Y	30	222534	266.90	7.42	18045 ± 765	4.70
^{94}Sr	30	425	1427.70	94.42	2913 ± 68	4.35
^{94}Y	30	7173	918.74	56.00	45081 ± 257	4.48
^{95}Y	30	3829	954.00	15.80	6711 ± 145	4.65
			1324.00	4.91	2215 ± 98	5.81
			2175.60	7.00	1926 ± 63	5.08
			2632.40	4.76	944 ± 40	4.32
			3576.00	6.38	1023 ± 34	4.89
^{97}Zr	577	242902	1149.97	2.62	9894 ± 240	5.95
			355.40	2.09	7902 ± 687	5.90
^{99}Mo	577	242902	777.92	4.28	8320 ± 428	4.65
^{99m}Tc	577	242902	140.51	89.00	39715 ± 850	4.36
^{101}Mo	30	5528	191.92	18.21	5925 ± 326	5.38
			1304.00	2.71	1646 ±103	5.36
			1599.26	1.75	919 ±80	5.38
^{101}Tc	30	10335	306.83	88.70	105166 ± 462	5.61
^{104}Tc	334	7963	358.00	89.00	41397 ± 341	3.62
			1612.40	5.79	1929 ± 85	3.22
			1596.70	4.18	1414 ± 82	3.25
^{105}Ru	2765	95852	316.44	11.12	15466 ± 510	2.77
			262.83	6.58	7300 ± 536	2.63
			413.53	2.27	4035 ± 441	2.98
^{105}Rh	577	242902	318.90	19.10	25015 ± 728	2.78
^{128}Sn	30	21214	482.30	59.00	14261 ± 336	0.57
			557.30	16.52	4119 ± 303	0.58
^{128}Sb	5562	237917	754.00	100.00	13089 ± 417	0.20
			314.10	61.00	6821 ± 685	0.22
^{128m}Sb	30	3829	753.90	96.40	14579 ± 200	1.61

			314.00	88.69	13222 ± 283	2.03
^{129}Sb	30	94940	812.80 683.50	47.60 5.66	35168 ± 345 4447 ± 358	1.09 1.11
^{130}Sn	30	1336	780.50	56.43	875 ± 119	0.47
^{130}Sb	3616	14224	793.40 839.52 182.33 732.00	100.00 100.00 65.00 22.00	8827 ± 176 9622 ± 169 2549 ± 306 2201 ± 172	0.74 0.83 0.82 0.83
^{131}Sb	334	7963	943.40 933.10 1207.4 854.6	46.20 25.87 3.88 3.23	19388 ± 190 12628 ± 177 1463 ± 121 1465 ± 158	2.38 2.79 2.38 2.50
^{131m}Te	30	243449	793.75	14.10	6057 ± 412	0.70
^{132}Te	2400	241079	228.33	88.12	85431 ± 849	4.71
^{132}I	30	243449	954.55 630.19 727.20	17.57 13.32 3.16	29802 ± 331 24867 ± 523 5752 ± 456	4.88 4.86 4.85
^{133}Sb	30	1336	1096.22	43.00	2165 ± 96	2.59
^{133m}Te	30	28933	912.67 647.51 863.96 914.77 978.30 1683.23	55.27 19.40 15.64 10.94 4.86 4.15	70144 ± 325 30434 ± 341 19427 ± 249 13995 ± 222 6903 ± 193 3837 ± 108	3.17 3.63 3.04 3.20 3.66 3.23
^{134}Te	30	15015	565.99 435.06 210.46 461.00 464.64	18.60 18.90 22.40 10.60 5.03	36590 ± 333 32642 ± 355 22979 ± 428 19492 ± 330 9270 ± 313	5.38 5.00 5.84 5.24 5.24
^{134}I	30	33918	847.03 884.09 1072.55 595.36 1136.16 857.29 947.86 1741.49	95.70 65.08 14.93 11.10 9.09 6.70 4.01 2.57	386358 ± 659 262124 ± 551 53751 ± 284 47620 ± 380 33235 ± 246 26628 ± 270 16365 ± 221 7312 ± 120	7.28 7.38 6.97 7.24 7.40 7.15 7.77 7.62
^{135}I	30	142104	1260.41 1131.51 1457.56 1678.03 1791.20	28.70 22.59 8.67 9.56 7.72	103434 ± 363 84064 ± 355 26695 ± 209 28593 ± 197 21157 ± 169	5.93 5.80 5.50 5.98 5.74
^{135m}Xe	30	147578	526.57	80.84	64938 ± 553	1.32
^{138}Xe	30	5228	2015.82	12.25	3750 ± 84	3.75
^{138}Cs	30	17081	1435.86 1009.78 2218.00 871.8	76.30 29.83 15.18 5.11	130311 ± 375 61012 ± 293 17644 ± 144 10134 ± 210	5.95 5.96 5.54 5.32
^{140}Cs	30	425	602.36	52.80	2335 ± 106	5.65
^{140}La	577	242902	1596.20 487.02 815.78 328.76	95.40 46.10 23.72 20.8	68089 ± 285 47606 ± 621 25183 ± 403 14948 ± 714	5.72 5.72 5.72 5.71
^{141}Ba	152	6443	190.33 343.67 457.80 462.30	46.00 14.44 5.01 4.88	14922 ± 347 9776 ± 292 3560 ± 249 3471 ± 248	4.69 4.97 4.45 4.44
^{142}Ba	30	3829	255.30 895.20 1204.30	20.50 13.86 14.23	6593 ± 291 6072 ± 152 5082 ± 129	5.00 4.59 4.21

			1078.70 949.10 1001.20 231.61 425.04 1202.40	11.46 10.60 9.72 12.12 5.72 5.54	4190 ± 128 4120 ± 134 4019 ± 134 3410 ± 293 2478 ± 232 1979 ± 114	4.09 4.13 4.52 4.96 4.52 4.21
^{142}La	30	36592	641.28 1363.00	47.40 2.13	139288 ± 483 4832 ± 140	4.89 4.95
^{143}Ce	5075	238404	293.27 664.57 721.93	42.80 5.69 5.39	82517 ± 760 15052 ± 453 14039 ± 431	4.41 4.36 4.36
^{146}Pr	4893	8693	453.88 1524.73 735.72	48.00 15.60 7.49	5991 ± 197 1435 ± 65 951 ± 134	5.90 5.89 5.87

It is worth noting that we provide cumulative yields for some ^{238}U photofission products that are not available in prior publications, namely ^{90m}Rb, ^{90}Rb, ^{99m}Tc, ^{128m}Sb, ^{130}Sn, ^{133}Sb, ^{140}Cs and ^{140}La. Most photofission product yields obtained in this work are in good agreement with existing data, but they are in average 25 % lower than those provided by Carrel *et al.* [6], in spite of a similar experimental configuration in terms of LINAC characteristics. The observed discrepancies in the published cumulative photofission yields can be due to several factors. In our case, analyzing several gamma-ray lines for a same photofission product, when possible, and observing a good consistency in the obtained yields enhances the reliability on the weighted average reported in the above tables (for example ^{87}Kr, ^{88}Kr, ^{134}I, ^{135}I, ^{138}Xe, ^{138}Cs, ^{142}La). In addition, correcting the fraction of neutron fissions with respect to photofissions thanks to MCNP improves the estimation of the absolute photofission yields. Other causes of discrepancy between published data are certainly due to differences in experimental configurations, such as the geometry of the samples, energy spectrum of the interrogating photon beam, photoneutron production, measurement sequence (irradiation, cooling and counting times), etc.

The ^{235}U cumulative photofission yields measured with the HEU sample are given in Table 10. The HEU sample mass being approximately two orders of magnitude smaller than that of the DU sample, counting statistics is not as good and fewer photofission products cumulative yields could be determined for ^{235}U.

666 *Table 10: Cumulative yields (per 100 fissions) for the photofission of ^{235}U and comparison with published data*

Photon beam type		Bremsstrahlung	Bremsstrahlung	Monoenergetic
Energy (MeV)		15.8	16.3	13.0
Fission product	**$T_{1/2}$**	**This work**	**Carrel 2011 [6]**	**Krishichayan 2019 [11]**
^{87}Kr	1.3 h	4.64 ± 0.74	-	3.45 ± 0.28
^{88}Kr	2.8 h	5.34 ± 0.84	3.63 ± 0.32	3.87 ± 0.22
^{89}Rb	15.4 min	6.89 ± 1.08	4.69 ± 0.28	-
^{91}Sr	9.7 h	7.71 ± 1.18	5.37 ± 0.26	6.08 ± 0.26
^{91m}Y	49.7 min	4.80 ± 1.72	5.38 ± 0.25	-
^{92}Sr	2.6 h	7.92 ± 1.24	5.59 ± 0.26	6.52 ± 0.21
^{92}Y	3.5 h	9.01 ± 2.44	-	-
^{93}Sr	7.4 min	8.02 ± 1.53	5.81 ± 0.27	-
^{93}Y	10.2 h	8.19 ± 2.53	-	6.14 ± 0.93
^{104}Tc	18.3 min	1.52 ± 0.24	-	2.37 ± 0.14
^{105}Ru	4.4 h	1.86 ± 0.29	-	1.90 ± 0.11
^{128}Sn	59.1 min	1.38 ± 0.22	-	1.22 ± 0.16
^{128}Sb	9 h	0.90 ± 0.14	0.39 ± 0.02	-
^{129}Sb	4.4 h	2.46 ± 0.36	1.60 ± 0.08	2.47 ± 0.12
^{130}Sb	39.5 min	1.49 ± 0.25	1.12 ± 0.05	0.82 ± 0.06
^{131}Sb	23 min	3.42 ± 0.53	2.75 ± 0.13	1.59 ± 0.13
^{131m}Te	1.3 d	1.98 ± 0.33	-	-
^{134}Te	41.8 min	5.33 ± 0.84	3.16 ± 0.15	5.37 ± 0.39
^{134}I	52.5 min	7.52 ± 2.22	-	-
^{135}I	6.6 h	7.34 ± 1.14	5.06 ± 0.32	4.72 ± 0.21
^{138}Xe	14.1 min	7.36 ± 1.18	4.62 ± 0.41	-
^{138}Cs	33.4 min	7.79 ± 2.61	-	7.74 ± 0.33
^{141}Ba	18.3 min	6.92 ± 1.06	-	4.43 ± 0.27
^{142}Ba	10.6 min	5.98 ± 1.06	4.41 ± 0.21	-
^{142}La	1.5 h	6.39 ± 2.18	5.15 ± 0.24	5.98 ± 0.19
^{143}Ce	1.4 d	6.41 ± 0.99	-	4.78 ± 0.30

667

668 *Table 11: Detailed data of the delayed gamma-ray analysis for each ^{235}U photofission product*

Fission Product	Cooling time (s)	Counting time (s)	Gamma-ray energy (keV)	Relative intensity (%)	Net peak area (counts)	Photofission cumulative yield (%)
^{87}Kr	392	27479	402.59 845.44 2554.80	49.60 7.34 9.23	10621 ± 147 731 ± 69 370 ± 25	4.66 4.15 4.45
^{88}Kr	30	61289	2392.11 834.83 165.98 1529.77 2035.41 2231.77	34.60 12.97 3.10 10.93 3.74 3.39	2535 ± 55 2234 ± 88 1575 ± 246 1124 ± 53 298 ± 36 249 ± 31	5.54 5.16 5.15 4.47 4.53 5.72
^{89}Rb	934	6689	1248.20	45.60	880 ± 43	6.89
^{91}Sr	392	79187	1024.30 749.80 652.90 652.30	33.50 23.68 8.04 2.98	6820 ± 101 6493 ± 121 2296 ± 120 851 ± 113	7.62 7.92 7.34 7.34
^{91m}Y	30	79549	555.57	95.00	20125 ± 181	4.80
^{92}Sr	30	61289	1383.90 430.48	93.00 3.35	15870 ± 134 1506 ± 128	7.92 7.65
^{92}Y	30	79549	934.50	13.90	4358 ± 92	9.01
^{93}Sr	30	3797	168.50 888.13	18.43 22.10	1614 ± 118 610 ± 50	8.08 7.95
^{93}Y	30	79549	266.90	7.42	4946 ± 188	8.19
^{104}Tc	392	7954	358.00	89.00	2219 ± 98	1.52
^{105}Ru	2742	79837	724.30 469.37 316.44 676.36	47.30 17.55 11.12 15.66	3206 ± 102 1742 ± 115 1866 ± 152 1042 ± 105	1.83 1.83 2.20 1.69
^{128}Sn	30	21152	482.30 557.30	59.00 16.52	2967 ± 111 705 ± 95	1.38 1.34
^{128}Sb	5635	73944	314.10 743.30 754.00 526.50	61.00 100.00 100.00 45.00	3968 ± 150 2788 ± 91 2540 ± 88 1627 ± 101	0.99 0.91 0.84 0.87
^{129}Sb	30	79549	812.80 544.70 1030.00	47.60 18.09 13.33	4025 ± 101 2746 ± 126 960 ± 70	2.31 2.95 2.40
^{130}Sb	3646	14282	182.33 330.91 793.40 839.52	65.00 78.00 100.00 100.00	1963 ± 123 1713 ± 94 777 ± 54 864 ± 52	1.66 1.60 1.22 1.42
^{131}Sb	392	7954	943.40 933.10	46.20 25.87	1404 ± 58 632 ± 52	3.57 2.82
^{131m}Te	30	79549	773.67 852.21	39.51 21.40	1416 ± 95 572 ± 79	2.08 1.45
^{134}Te	30	15005	277.95 767.20 201.24 565.99	21.30 29.60 8.90 18.60	5444 ± 144 3249 ± 89 2502 ± 150 2509 ± 98	5.31 5.51 4.97 5.18
^{134}I	30	33988	884.09 595.36 405.45 857.29	65.08 11.10 7.37 6.70	13413 ± 133 3487 ± 112 3180 ± 128 1526 ± 78	7.45 8.38 8.09 8.28
^{135}I	30	79549	1260.41 1131.51 288.45 836.80	28.70 22.59 3.10 6.69	5217 ± 89 4657 ± 91 2153 ± 176 1704 ± 86	7.23 7.49 7.81 7.21

			1457.56 1678.03 1791.20	8.67 9.56 7.72	1496 ± 58 1316 ± 53 997 ± 47	7.84 7.05 6.95
^{138}Xe	30	5243	258.41 1768.26 2015.82	31.50 16.73 12.25	4479 ± 121 390 ± 33 293 ± 28	7.48 6.27 7.32
^{138}Cs	30	16994	1435.86 2218.00 2639.59	76.30 15.18 7.63	7856 ± 96 1060 ± 40 448 ± 26	7.79 7.78 7.85
^{141}Ba	211	6327	304.19	25.44	3441 ± 109	6.92
^{142}Ba	30	3797	985.20	13.86	411 ± 49	5.98
^{142}La	30	36519	894.90 2397.80	8.34 13.27	1499 ± 76 998 ± 38	6.40 6.38
^{143}Ce	5092	74487	293.27	42.80	9883 ± 170	6.41

Despite the abovementioned limitations in terms of counting statistics, we provide here cumulative yields for some ^{235}U photofission products that are not reported in prior publications, namely ^{92}Y, ^{131m}Te and ^{134}I. For the others, the cumulative yields obtained in this work are quite consistent with existing data, but contrary to ^{238}U for which our yields were a bit smaller than in previous references, they are now a bit larger. For instance, we observe an average difference of 28 % with Carrel *et al.* [6], despite a similar LINAC configuration as in our experiments as already reported. The origin of possible biases in our experiments with DU and HEU samples will be further investigated by using another HEU sample with a larger mass, which will also allow measuring more ^{235}U yields.

4.3. ^{235}U / ^{238}U discrimination from gamma-ray lines ratios

When photofission occurs, the formation of two asymmetric fission fragments is the most likely to happen, resulting in a mass distribution curve of the fission products comporting two bumps: one for a heavy nucleus centered around mass number 140, and one for a light nucleus centered around 95. Examples of this theoretical mass distribution for photofission products are given in ref. [34] for several actinides. A discrimination information can be obtained between uranium isotopes thanks to their different photofission product yields, and thus the intensity difference in their delayed gamma spectra [1][14]. The ^{235}U enrichment can thus be computed from photofission delayed gamma ratios of the net areas and from the respective ^{235}U and ^{238}U photofission yields ratios of specific photofission product pairs. The efficiency of this discrimination method can be assessed by defining a discrimination criterion based on the difference of photofission yields ratios from any photofission product to any other. By maximizing this

discrimination criterion $\delta = \left[\frac{Y_{5,PF1}}{Y_{8,PF1}} - \frac{Y_{5,PF2}}{Y_{8,PF2}}\right]$, the most appropriate photofission product couples can be identified based on the cumulative photofission product yields we reported in previous section. These pairs of photofission products with the largest values of δ are given in Table 12.

Table 12: Photofission products offering the best capability for ^{235}U vs. ^{238}U discrimination (see the text for the definition of δ)

Fission product couple	δ
^{128}Sb/^{104}Tc	3.86
^{128}Sb/^{105}Ru	3.61
^{128}Sb/^{134}Te	3.28
^{128}Sb/^{134}I	3.26
^{128}Sb/^{135}I	3.03
^{128}Sb/^{142}La	2.98
^{128}Sb/^{138}Cs	2.97
^{128}Sb/^{131}Sb	2.92
^{128}Sb/^{142}Ba	2.92
^{128}Sb/^{141}Ba	2.83

It appears that ^{128}Sb is part of all fission product couples because of its particularly high ratio between its cumulative yields for ^{235}U and ^{238}U. However, the value of its cumulative photofission yield measured in this work for ^{235}U is more than two times higher than the only value previously published by Carrel *et al.* [6]. Improved counting statistics for ^{235}U will enable to verify this particular yield and eventually to update the most discriminating pairs of photofission products in future work. Besides, it should be noted that the fission product couples listed above are not equally applicable to practical measurements. Indeed, the energy dependence of detection efficiency and gamma-ray attenuation, due to the waste matrix, for instance, as well as gamma-ray interferences and the experimental sequence (irradiation, cooling, counting times), have to be taken into account to select the relevant fission product couples for a given application. This selection will be refined in future work aiming at developing a practical method to characterize nuclear materials in large radioactive waste packages using photofission.

5. Conclusion

New measurements of cumulative photofission yields with a 15.8 MeV endpoint Bremsstrahlung photon beam produced by a SATURNE electron LINAC have been performed in CINPHONIE facility, at CEA Cadarache, France. To this aim, a characterization of the Bremsstrahlung photon beam has been first carried out by photon activation analysis with different samples of Au, Ni, U and Zr. Then, the residual neutron flux exiting the LINAC head (lead collimator, borated polyethylene and cadmium shield) has been characterized by neutron activation analysis with Au, In, Cu, Ni and Mg samples (mostly In activation gamma rays), so as to estimate the contribution of photoneutron fissions in the DU and HEU samples used to assess the photofission yields. The impact of photoneutrons produced in the LINAC and its surroundings (tungsten target, lead collimator, cadmium sheet) is limited for this type of experiment, most of neutron fissions arising from fast neutrons produced in the sample itself. Finally, the cumulative production yields of 49 and 26 photofission products have been measured for ^{238}U and ^{235}U, respectively, from which 8 and 3 yields were not reported so far in the literature. Some photofission products, showing large discrepancies between both uranium isotopes appear as good candidates for an isotope discrimination method based on gamma-ray lines ratios measurement.

The preparation of new experimental campaigns is underway, firstly to assess photofission products cumulative yields for other actinides of interest, like plutonium, and secondly to test the differentiation of actinides isotopes with a strong attenuation of photofission delayed gamma rays by a dense waste matrix, like concrete.

References

[1] F. Carrel, M. Agelou, M. Gmar, F. Lainé, J. Loridon, J.-L. Ma, C. Passard, B. Poumarède, *"Identification and Differentiation of Actinides Inside Nuclear Waste Packages by Measurement of Delayed Gammas"*, IEEE Trans. Nucl. Sci., 57 (5) 2862, (2010).

[2] F. Carrel, M. Agelou, M. Gmar, F. Lainé, *"Detection of high-energy delayed gammas for nuclear waste packages characterization"*, Nuclear Instruments and Methods in Physics Research, Section A, 652 (1), 137-139 (2011).

[3] T. Nicol, B. Pérot, C. Carasco, F. Brackx, A. Mariani, C. Passard, E. Mauerhofer, J. Collot, *"Feasibility study of ^{235}U and ^{239}Pu characterization in radioactive waste drums using neutron-induced fission delayed gamma rays"*, Nuclear Instruments and Methods in Physics Research, Section A, vol 832, 85-94 (2016).

[4] E. Simon, F. Jallu, B. Pérot, S. Plumeri, *"Feasibility study of fissile mass quantification by photofission delayed gamma rays in radioactive waste packages using MCNPX"*, Nuclear Instruments and Methods in Physics Research, Section A, vol 840, 28-35, (2016).

[5] S. Kahane, A. Wolf, *"Photofission of ^{238}U with neutron-capture gamma rays"*, Phys. Rev. C, vol 32 no 6, (1985).

[6] F. Carrel, M. Agelou, M. Gmar, F. Lainé, J. Loridon, J.-L. Ma, C. Passard, (...), B. Poumarède, *"New Experimental Results on the Cumulative Yields From Thermal Fission of ^{235}U and ^{239}Pu and From Photofission of ^{235}U and ^{238}U Induced by Bremsstrahlung"*, IEEE Transactions on Nuclear Science, 58, 2064-2072, (2011).

[7] H. Naik, V. T. Nimje, D. Raj, S. V. Suryanarayana, A. Goswami, S. Singh, S. N. Acharya, K. C. Mittal, S. Ganesan, P. Chandrachoodan, V. K. Manchanda, V. Venugopal, and S. Banarjee, *"Mass distribution in the bremsstrahlung-induced fission of ^{232}Th, ^{238}U and ^{240}Pu"*, Nucl. Phys. A 853, 1 (2011).

[8] H. Naik, F. Carrel, G. N. Kim, F. Laine, A. Sari, S. Normand, and A. Goswami, *"Mass yield distributions of fission products from photo-fission of ^{238}U induced by 11.5-17.3 MeV bremsstrahlung"*, Eur. Phys. J. A 49, 94 (2013).

[9] H. Naik, B. S. Shivashankar, H. G. Raj Prakash, D. Raj, G. Sanjeev, N. Karunakara, H. M. Somashekarappa, S. Ganesan, G. N. Kim, and A. Goswami, *"Measurements of fission yield in 8 MeV bremsstrahlung induced fission of ^{232}Th and ^{238}U"*, J. Radioanal. Nucl. Chem. 299, 127 (2014).

[10] X. Wen and H. Yang, *"Photofission product yields of ^{238}U and ^{239}Pu with 22-MeV bremsstrahlung"*, Nuclear Instruments and Methods in Physics Research Section A, Volume 821, 34 (2016).

[11] Krishichayan, Megha Bhike, C. R. Howell, A. P. Tonchev, and W. Tornow, *"Fission product yields measurements using monoenergetic photon beams"*, Physical Review C 100, 014608 (2019).

[12] C. L. Hollas, D. A. Close, C. E. Moss, *"Analysis of fissionable material using delayed gamma rays from photofission"*, Nuclear Instruments and Methods in Physics Research, Section B, vol 24-25, Part 1, 503-505 (1987).

[13] D. H. Beddingfield and F. E. Cecil, *"Identification of fissile materials from fission product gamma-ray spectra"*, Nuclear Instruments and Methods in Physics Research, Section A, vol. 417, 405-412 (1998).

[14] M. Gmar, J.M. Capdevila, *"Use of delayed gamma spectra for detection of actinides (U,Pu) by photofission"*, Nuclear Instruments and Methods in Physics Research Section A 422, 841-845 (1999).

[15] B. Pérot, F. Jallu, C. Passard, O. Gueton, P.-G. Allinei, L. Loubet, N. Estre, E. Simon, C. Carasco, C. Roure, L. Boucher, H. Lamotte, J. Comte, M. Bertaux, A. Lyoussi, P. Fichet and F. Carrel, *"The characterization of radioactive waste: a critical review of techniques implemented or under development at CEA, France"*, EPJ Nuclear Sciences and Technologies 4, 3 (2018)

[16] IAEA, "Handbook on photonuclear data for applications – Cross-sections and spectra", TECDOC-1178 (2000)

[17] D.A. Brown, *et al.*, *"ENDF/B-VIII.0: The 8th Major Release of the Nuclear Reaction Data Library with CIELO-project Cross Sections, New Standards and Thermal Scattering Data"*, Nucl. Data Sheets 148, 1-142 (2018).

[18] N. Estre, D. Eck, J.-L. Pettier, E. Payan, C. Roure, E. Simon, *"High-Energy X-Ray Imaging Applied to Nondestructive Characterization of Large Nuclear Waste Drums",* IEEE Transactions on Nuclear Science 62:6, 3104-3109 (2015).

[19] Abul Kalam Md, L. Rahman, K. Kato, H. Arima, N. Shigyo, K. Ishibashi, J. Hori, K. Nakajima, *"Study on Effective Average (γ,n) Cross Section for ^{89}Y, ^{90}Zr, ^{93}Nb and ^{133}Cs and (γ,3n) Cross Section for ^{99}Tc"*, Journal of Nuclear Science and Technology, 47:7, 618-625 (2010).

[20] H. Naik, S. V. Suryanarayana, K. C. Jagadeesan, S. V. Thakare, P. V. Josh, (…), S. Kailas, *"An alternative route for the preparation of the medical isotope ^{99}Mo from the ^{238}U(γ,f) and ^{100}Mo(γ,n) reactions"*, J. Radioanal. Nucl. Chem. 295, 807-816 (2013).

[21] M. Bhike, W. Tornow, Krishichayan, A.P. Tonchev, *"Exploratory study of fission product yield determination from photofission of ^{239}Pu at 11 MeV with monoenergetic photons"*, Phys. Rev. C 95, 024608 (2017).

[22] R. Nath, R.-J. Schulz, *"Determination of high-energy X-ray spectra by photoactivation"*, Medical Physics, vol. 3, no. 3, 133-141 (1975).

[23] A. J. M. Plompen, O. Cabellos, C. De Saint Jean *et al.* The joint evaluated fission and fusion nuclear data library, JEFF-3.3. Eur. Phys. J. A 56 181 (2020).

[24] Los Alamos National Laboratory, *Mcnp 6™ User's Manual*, Denise B. Pelowitz (2013).

[25] Thales Group, Private communication (2016).

[26] N. Otuka, E. Dupont, V. Semkova, B. Pritychenko, A. I. Blokhin, M. Aikawa, S. Babykina, M. Bossant, G. Chen, S. Dunaeva, R. A. Forrest, T. Fukahori, N. Furutachi, S. Ganesan, Z. Ge, O. O. Gritzay, M. Herman, S. Hlavač, K. Katō, B. Lalremruata, Y. O. Lee, A. Makinaga, K. Matsumoto, M. Mikhaylyukova, G. Pikulina, V. G. Pronyaev, A. Saxena, O. Schwerer, S. P. Simakov, N. Soppera, R. Suzuki, S. Takács, X. Tao, S. Taova, F. Tárkányi, V. V. Varlamov, J. Wang, S. C. Yang, V. Zerkin, Y. Zhuang, *"Towards a More Complete and Accurate Experimental Nuclear Reaction Data Library (EXFOR): International Collaboration Between Nuclear Reaction Data Centres (NRDC)"*, Nucl. Data Sheets 120, 272-276 (2014).

[27] C. Plaisir *et al.*, *"Measurement of the $^{85}Rb(\gamma, n)^{84m}Rb$ cross-section in the energy range 10–19 MeV with bremsstrahlung photons"*, Eur. Phys. Journal A 48:68 (2012). (EXFOR G0033.002)

[28] H. Choudens, G. Troesch, *« Radioprotection dans les installations nucléaires »*, ISBN 978-2743001469 (1997).

[29] A-C. Simon, J-P. Both, I. Espagnon, J. Lefevre, V. Picaud, A. Pluquet, *"A new computer code for the determination of the isotopic composition of actinides by X- and gamma-ray spectrometry and its applications"*, European Nuclear Conference 2005, France (2006).

[30] A-C. Simon, F. Carrel, I. Espagnon, M. Lemercier and A. Pluquet, *"Determination of Actinide Isotopic Composition: Performances of the IGA Code on Plutonium Spectra according to the Experimental Setup",* IEEE Transactions on Nuclear Science, vol 58, no 2 (2011).

[31] H. Bateman, *"The solution of a system of differential equations occurring in the theory of radioactive transformations"*, Proc. Cambridge Philosophical Society, vol. 15, 423-427 (1910).

[32] J. Katakura, *JENDL FP Decay Data File 2011 and Fission Yields Data File 2011*, Japan Atomic Energy Agency, (2012).

[33] P. Leconte, J. P. Hudelot and M. Antony, *"Accurate γ-ray spectrometry measurements of the half-life of ^{92}Sr"*, Applied Radiation and Isotopes, vol. 66, issue 10, 1450-1458 (2008).

[34] D. Bernard, O. Sérot, E. Simon, L. Boucher and S. Plumeri, *"A Photofission Delayed γ-ray Spectra Calculation Tool for the Conception of a Nuclear Material Characterization Facility"*, EPJ Web of Conferences 170, 06001 (2018).

Highlights

- Photofission is a promising technique to assay nuclear waste packages
- Photon activation analysis is used to characterize a 16 MeV Bremsstrahlung beam
- New photofission products cumulative yields have been determined for ^{235}U and ^{238}U
- Special attention has been drawn to distinguish neutron fission from photofission
- Photofission product yield difference makes actinides differentiation practicable

CRediT author statement:

M. Delarue: Methodology, Investigation, Software, Writing – Original Draft, Visualization, Formal analysis

E. Simon: Conceptualization, Methodology, Writing – Review & Editing

B. Pérot: Supervision, Writing – Review & Editing

P.G. Allinei: Software, Investigation, Resources

N. Estre: Investigation, Resources

E. Payan: Investigation, Resources

E. Eck: Investigation, Resources

D. Tisseur: Investigation, Resources

I. Espagnon: Software

J. Collot: Supervision, Writing – Review & Editing

Declaration of interests

☒ The authors declare that they have no known competing financial interests or personal relationships that could have appeared to influence the work reported in this paper.

☐The authors declare the following financial interests/personal relationships which may be considered as potential competing interests: